Title
Remote sensing of clouds for solar forecasting applications

Author
Mejia, Felipe Alejandro

Publication Date
2017

UNIVERSITY OF CALIFORNIA, SAN DIEGO

Remote sensing of clouds for solar forecasting applications

A dissertation submitted in partial satisfaction of the
requirements for the degree
Doctor of Philosophy

in

Engineering Sciences (Mechanical Engineering)

by

Felipe Mejia

Committee in charge:

Professor Jan Kleissl, Chair
Professor Carlos Coimbra
Professor Amato Evan
Professor Joel Norris
Professor George Tynan

2017

The dissertation of Felipe Mejia is approved, and it is acceptable in quality and form for publication on microfilm and electronically:

Chair

University of California, San Diego

2017

DEDICATION

This work is dedicated to my family.

TABLE OF CONTENTS

LIST OF FIGURES

LIST OF TABLES

ACKNOWLEDGEMENTS

I would like to thank Professor Jan Kleissl for his support during my research. I am extremely grateful for working and learning from all of my labmates: Andu Nguyen, Ben Kurtz, Bryan Urquhart, Matthew Lave, Patrick Mathiesen, Mohamed Ghonima, Janet Shields, Handa Yang, Iman Gohari, Juan Bosch, Elliot Dahlin, Guang Wang, Oytun Babacan, Ryan Hanna, Xiaohui Zhong, Keenan Murray, Zack Pecenak. This research would also not be possible without the vital contributions to the development and production of the sky imager of Caspar Hanselaar, Edmundo Godinez, William Gui, Prithvi Sundar, Dan Erez, Scott Kato, Amy Chiang, Jessica Traynor, Kristen Ostosh, Tyler Capps, Sebastian Schwarz- fischer, Sebastian Pangratz, Christian Faltermeier, Nick Truong, Salil Kektar, Jeff Yeh, Max Twogood, Alex Turchik, Danielle Donnely, Emily Davis, Victor Fung, Victor Piovano, Eric Quaal, Eddie Lin, Anthony Tran, Ryan Gillespie and Brandon Jacoby.

Chapters 1-3, in part, contains material as it appears in F. A. Mejia, B. Kurtz, K. Murray, L. M. Hinkelman, M. Sengupta, Y. Xie, and J. Kleissl, Coupling sky images with radiative transfer models: a new method to estimate cloud optical depth, Atmospheric Measurement Techniques, vol. 9, iss. 8, pp. 4151-4165, 2016. The dissertation author was the primary researcher and author of this material.

Chapter 4 is currently in being prepared for submission for publication of the material. F. A. Mejia, B. Kurtz, and J. Kleissl, Cloud tomography applied to sky images: Part I: A virtual testbed. The dissertation author was the primary researcher and author of this material.

Chapter 5 is currently in being prepared for submission for publication of the material. F. A. Mejia, B. Kurtz, and J. Kleissl, Cloud tomography applied to sky images: Part II: A real world case study. The dissertation author was the primary researcher and author of this material.

VITA

2012	B. S. in Mechanical Engineering and Material Science, Duke University
2012-2014	Master of Science, University of California, San Diego
2017	Doctor of Philosophy, University of California, San Diego

PUBLICATIONS

F. A. Mejia, B. Kurtz, and J. Kleissl, Cloud tomography applied to sky images: Part I: A virtual testbed. In preparation.

F. A. Mejia, B. Kurtz, and J. Kleissl, Cloud tomography applied to sky images: Part II: A real world case study. In preparation.

F. A. Mejia, B. Kurtz, K. Murray, L. M. Hinkelman, M. Sengupta, Y. Xie, and J. Kleissl, Coupling sky images with radiative transfer models: a new method to estimate cloud optical depth, Atmospheric Measurement Techniques, vol. 9, iss. 8, pp. 4151-4165, 2016.

F. A. Mejia and J. Kleissl, Soiling losses for solar photovoltaic systems in California, Solar Energy, vol. 95, pp. 357-363, 2013.

F. A. Mejia, J.L. Bosch and J. Kleissl, The effect of dust on solar photovoltaic systems, Energy Procedia, vol. 49, pp. 2370-2376, 2014.

B. Kurtz, **F. A. Mejia** and J. Kleissl, ”A virtual sky imager testbed for solar energy forecasting,” Solar Energy, vol. 158, 753-759.

M. Lave, J. Keissl, A. Ellis, **F. A. Mejia**, Simulated PV power plant variability: Impact of utility-imposed ramp limitations in Puerto Rico, Photovoltaic Specialists Conference (PVSC), 2013 IEEE 39th, pp. 1817-1821, 2013.

Z. K. Pecenak, **F. A. Mejia**, B. Kurtz, A. Evan and J. Kleissl, Simulating irradiance enhancement dependence on cloud optical depth and solar zenith angle, Solar Energy, vol. 136, pp. 675-681, 2016.

ABSTRACT OF THE DISSERTATION

Remote sensing of clouds for solar forecasting applications

by

Felipe Mejia

Doctor of Philosophy in Engineering Sciences (Mechanical Engineering)

University of California, San Diego, 2017

Professor Jan Kleissl, Chair

A method for retrieving cloud optical depth (τ_c) using a UCSD developed ground-based Sky Imager (USI) is presented. The Radiance Red-Blue Ratio (RRBR) method is motivated from the analysis of simulated images of various τ_c produced by a Radiative Transfer Model (RTM). From these images the basic parameters affecting the radiance and RBR of a pixel are identified as the solar zenith angle (SZA), τ_c, solar pixel angle/scattering angle (SPA), and pixel zenith angle/view angle (PZA). The effects of these parameters are described and the functions for radiance, $I_\lambda(\tau_c, SZA, SPA, PZA)$, and the red-blue ratio, $RBR(\tau_c, SZA, SPA, PZA)$, are retrieved from the RTM results. RBR, which is commonly used for cloud detection in sky images, provides non-unique solutions for

τ_c, where RBR increases with τ_c up to about $\tau_c = 1$ (depending on other parameters) and then decreases. Therefore, the RRBR algorithm uses the measured $I_\lambda^{meas}(SPA, PZA)$, in addition to $RBR^{meas}(SPA, PZA)$ to obtain a unique solution for τ_c. The RRBR method is applied to images of liquid water clouds taken by a USI at the Oklahoma Atmospheric Radiation Measurement program (ARM) site over the course of 220 days and compared against measurements from a microwave radiometer (MWR) and output from the Min [MH96a] method for overcast skies. τ_c values ranged from 0-80 with values over 80 being capped and registered as 80. A τ_c RMSE of 2.5 between the Min method [MH96b] and the USI are observed. The MWR and USI have an RMSE of 2.2 which is well within the uncertainty of the MWR. The procedure developed here provides a foundation to test and develop other cloud detection algorithms.

Using the RRBR τ_c estimate as an input we then explore the potential of using tomographic techniques for 3-D cloud reconstruction. The Algebraic Reconstruction Technique (ART) is applied to optical depth maps from sky images to reconstruct 3-D cloud extinction coefficients. Reconstruction accuracy is explored for different products, including surface irradiance, extinction coefficients and Liquid Water Path, as a function of the number of available sky imagers (SIs) and setup distance. Increasing the number of cameras improves the accuracy of the 3-D reconstruction: For surface irradiance, the error decreases significantly up to four imagers at which point the improvements become marginal while k error continues to decrease with more cameras. The ideal distance between imagers was also explored: For a cloud height of 1 km, increasing distance up to 3 km (the domain length) improved the 3-D reconstruction for surface irradiance, while k error continued to decrease with increasing decrease. An iterative reconstruction technique was also used to improve the results of the ART by minimizing the error between input images and reconstructed simulations. For the best case of a nine imager deployment, the ART and iterative method resulted in 53.4% and 33.6% mean

average error (MAE) for the extinction coefficients, respectively.

The tomographic methods were then tested on real world test cases in the University of California San Diego's (UCSD) solar testbed. Five UCSD sky imagers (USI) were installed across the testbed based on the best performing distances in simulations. Topographic obstruction is explored as a source of error by analyzing the increased error with obstruction in the field of view of the horizon. As more of the horizon is obstructed the error increases. If at least a field of view of 70° is available for the camera the accuracy is within 2% of the full field of view. Errors caused by stray light are also explored by removing the circumsolar region from images and comparing the cloud reconstruction to a full image. Removing less than 30% of the circumsolar region image and GHI errors were within 0.2% of the full image while errors in k increased 1%. Removing more than 30° around the sun resulted in inaccurate cloud reconstruction. Using four of the five USI a 3D cloud is reconstructed and compared to the fifth camera. The image of the fifth camera (excluded from the reconstruction) was then simulated and found to have a 22.9% error compared to the ground truth.

Chapter 1

Introduction

1.1 Motivation: The Need for Solar Forecasting

The transition from conventional fossil energy to renewable energy has been aided by continued improvements in renewable technologies, but this progress is met with new challenges. Solar energy, for example, has an inherent variability that unlike current energy sources, that provide a steady reliable energy source, requires larger regulation by ancillary generators to balance generation and demand during periods of high variability. Accurate forecasting of these periods of high variability will support management of the electric grid and electricity markets and therefore ensure a more economical integration of solar power (Mathiesen et al., 2013). Currently several different methods are used to forecast at different spatial and temporal resolutions including numerical weather prediction (e.g. Lorenz et al., 2009; Mathiesen et al., 2011), and satellite image-based forecasting (e.g. Hammer et al., 1999). For short term forecasting, whole-sky imagery has been used (e.g. Urquhart et al., 2013).

1.2 The need for improvements in cloud detection

Physics-based solar forecasting using whole-sky imagery requires geolocating clouds in the sky images, estimating their optical depth, motion, and dynamics (Chow et al., 2011). To estimate a clouds optical depth τ_c, the most advanced methods separate the image into clear sky, thin cloud and thick cloud and assign a τ_c to each of these groups. To distinguish thin and thick clouds, the red-blue ratio (RBR) (or a function of RBR) has been used as the default method (Koehler et al., 1991; Shields et al., 1993; Chow et al., 2011; Ghonima et al. 2012; Roy et al., 2001). It is defined as the ratio of the signal from the red channel to the signal from the blue channel. The RBR method takes advantage of Rayleigh scattering being greater in the blue wavelengths than the red wavelengths. When Rayleigh scattering is the predominant form of scattering, such as in clear skies, the RBR for a given view angle is smaller than under cloud scattering. RBR successfully differentiates clear sky from thin clouds and to a more limited extent thick clouds, but the RBR has not been applied to differentiate τ_c. It is also difficult to apply the RBR method in the circumsolar region as thick dark clouds have lower RBRs than clear sky (Chow et al., 2011). In fact we will demonstrate through radiative transfer modeling (Chapter 3) that RBR by itself is ineffective for differentiating τ_c even for homogeneous cloud layers. Differences in τ_c can greatly affect the irradiance available for solar energy production. For this analysis we consider the of-accuracy requirement of global horizontal irradiance (GHI) to be 5% Fig. 1.1a. Fig. 1.1b and 1.1c demonstrate the corresponding absolute and relative error in τ_c for a 5% error in GHI. Relative τ_c accuracy required for solar forecasting is large for thin cloud ($\tau_c \sim 1$) and thick clouds ($\tau_c > 30$). A minimum occurs at τ_c=16 where a 21% error in τ_c is permissible for avoiding an under-prediction of GHI by 5%.

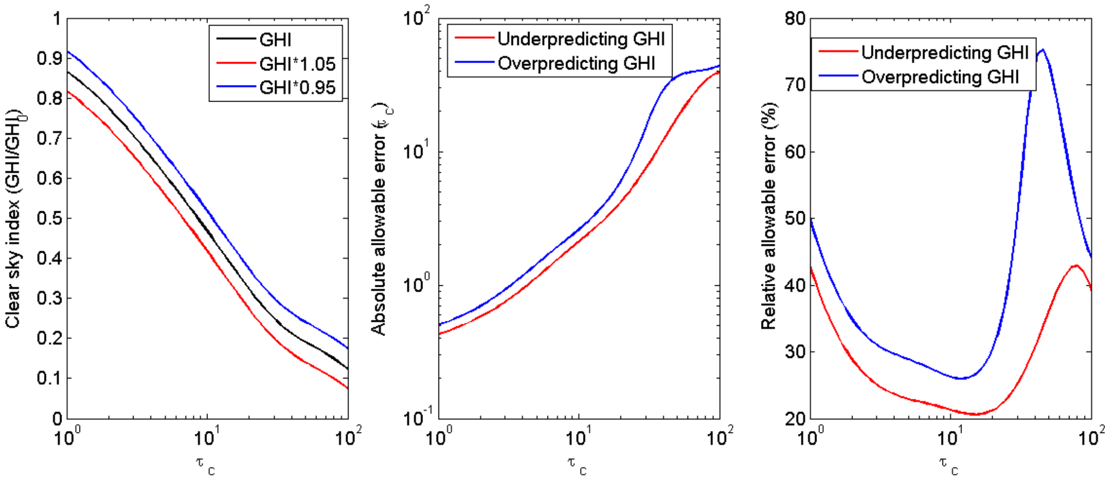

Figure 1.1: a) Irradiance divided by clear sky irradiance as a function of τ_c for homogenous clouds as derived from SHDOM. The black line represents the results while the blue and red are 5% offsets in GHI. 1.1b) Error bounds of 5% on 1.1a converted to absolute intervals for τ_c. For example, for GHI to stay within 5% of its value at τ_c=30, τ_c cannot be more than 7.7 below 30 and not more than 15.6 above 30. 1.1c) Same as 1.1b but the y-axis is divided by τ_c.

Most current cloud detection methods are designed empirically using look-up tables and/or thresholds that are adjusted to work with a specific imager and cloud conditions (see section 1.3). The present work breaks new ground in that it attempts to improve our fundamental understanding of the impact of radiative transfer (RT) and τ_c on the radiance and RBR of a given pixel in a sky image. To analyze this relation, the Spherical Harmonic Discrete Ordinate Method (SHDOM) (Evans et al., 1998; Pincus et al., 2009) is used to produce synthetic overcast sky images (chapter 2) and analyze the determinants of sky imager radiances (chapter 3). The results reveal non-linearities and non-monotonic behavior in radiances and RBR that explain many of the challenges previously observed with empirical cloud detection methods. The insights gained through RT are utilized to develop a τ_c retrieval algorithm for sky imagery (section 3.6). The algorithm is compared to other methods in section 3.9.

1.3 Review of sky imager cloud detection methods and geometrical factors

Individual pixel cloud detection using the output image from sky imagers is based on either the radiance measurement or the ratio between radiance measurements for different wavelengths. Cloud detection algorithms using single channel radiance have found limited success (McGuffe et al., 1989; Kegelmeyer et al., 1994) due to the similarities in radiance values between clear skies and thick clouds in the visible spectrum. More success has been obtained when cloud detection uses the ratio between radiance measurements at different wavelength bands. One such algorithm is the RBR method, which uses the ratio of camera measurement in the red channel to the blue channel to classify a pixel as cloudy or clear. A fixed RBR threshold between clear sky and cloudy sky (Koehler et al. 1991) led to successful identification of opaque clouds but consistently failed to distinguish thin and clear skies. However, in a study of contrail clouds Koehler et al. (1991) observed that the ratio of RBR to the clear sky RBR was similar between contrail cases and permitted a method for identifying thin clouds. In other words, knowing the clear sky value, aids in the detection of thin clouds. The main factors affecting the clear sky RBR were found to be the solar zenith angle (SZA, Fig. 1.2), solar pixel angle/scattering angle (SPA), pixel zenith angle/view angle (PZA, see Figs. 1.2, 1.3b, 1.3c for illustrations of these angles), and changes in aerosol properties. This lead to the development of clear sky libraries (CSL) (Shields et al.,1993; Chow et al. 2011) to express clear sky RBR value under any condition. CSL are constructed by binning pixel values from clear sky images into matrices as a function of SZA (Fig. 1.2), SPA and PZA. From the CSL it is then possible to simulate a clear sky (Fig. 1.3a) for any given day, allowing the calculation of the ratio of measured RBR to clear sky RBR.

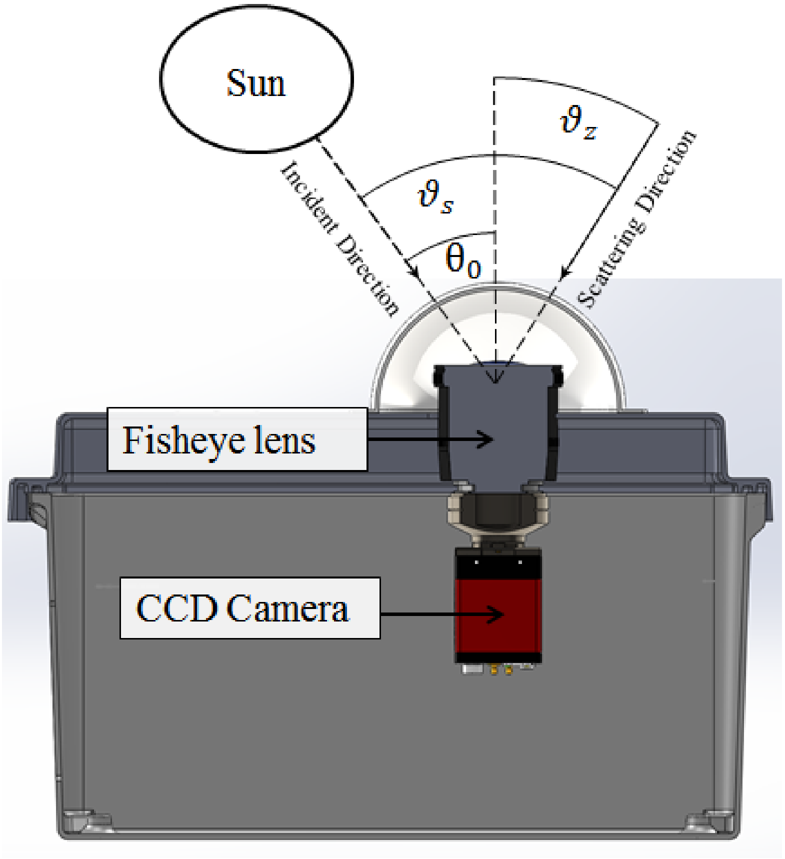

Figure 1.2: Diagram of the UCSD sky imager (USI) and related solar and sky geometries. SZA is the solar zenith angle. The SPA is the angle subtended by the vector pointing at the sun and the vector pointing at the pixel in question. The PZA is the angle formed by the vector pointing at the pixel in question and zenith. It is important to note that SPA = SZA+ PZA only holds in 2D, but not in 3D because the incident and scattering directions may not be in the same azimuthal plane. An example of this is illustrated in Fig. 1.3.

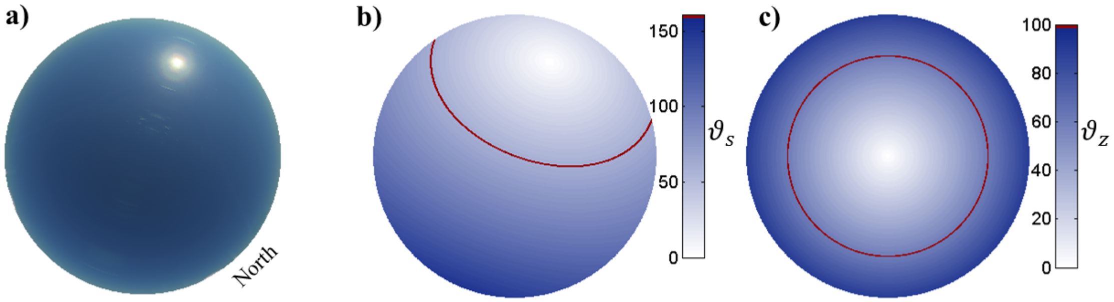

Figure 1.3: (a) Clear USI image created from a clear sky library (CSL) for a solar zenith angle of 60 on 26 March 2013, 15:00:00 UTC. For the image in (a) Solar Pixel Angles and Pixel Zenith Angles are shown in (b) and (c), respectively. The red lines in Figs b. and highlight the pixels with SPA=60, and PZA=60, respectively, which are often used in the following chapters to illustrate relationships with cloud optical depth and radiance. North is located on the bottom right corner of the image.

The red-blue difference (RBD, Heinle et al., 2010) uses the same principles as the RBR for cloud detection but attempts to eliminate the strong directional variability in the RBR due to variability in the radiance, $I_{\Delta\lambda}$, of the blue channel as seen in eqn. (1.1, 1.2) ,

$$RBR = \frac{I_r}{I_b} = 1 + \frac{(I_r - I_b)}{I_b}, \tag{1.1}$$

$$RBD = I_r - I_b = I_b(RBR - 1), \tag{1.2}$$

where I_r is the $I_{\Delta\lambda}$ in the red channel, and I_b is the $I_{\Delta\lambda}$ in the blue channel. However, Ghonima et al. (2012) found minimal differences in performance between RBD and RBR retrieval with RBR outperforming RBD. Gauchet et al. (2012) used RBD combined with a different approach to account for the directional effects in cloud detection, in which they segmented images into five zones, solar disk, circumsolar disk, extended circumsolar disk, main zone, sky horizon, and orographic horizon. The Radiance and red-blue difference (RBD) thresholds to separate clear sky, bright cloud, and dark cloud varied by zone. These approaches have led to improved accuracy of cloud detection, yet limited progress has been made towards understanding the phenomena that influence the performance of these methods. Although a direct relationship with aerosol optical depth (τ_a) and RBR is observed for small τ_a, ($\tau_a < 0.3$) (Ghonima et al., 2012) no direct relationship has been found between RBR, or other variables determined from sky imagers, and larger optical depths ($\tau > 0.3$) such as those found typically in clouds. This has limited sky imager cloud detection to a binary classification in which the image is segmented into cloud or clear sky. The lack of research on τ_c classification also stems from the fact that τ_c are challenging to measure accurately and large spatio-temporal variability. Instead, a radiative transfer model is applied here to investigate the interrelationships between radiances, radiance ratios (RBR), and τ_c and devise a method to detect τ_c.

Acknowledgements

Chapter 1, in part, contains material as it appears in F. A. Mejia, B. Kurtz, K. Murray, L. M. Hinkelman, M. Sengupta, Y. Xie, and J. Kleissl, Coupling sky images with radiative transfer models: a new method to estimate cloud optical depth, Atmospheric Measurement Techniques, vol. 9, iss. 8, pp. 4151-4165, 2016. The dissertation author was the primary researcher and author of this material.

Chapter 2

Homogeneous radiative transfer modeling of sky images and comparison to measurements

2.1 SHDOM model and input parameters

Radiance measurements can be obtained from a 1D model for homogeneous clouds but for comparison with future work a 3D-RT model was used. SHDOM is an explicit 3D-RT model that uses discrete ordinates to integrate the radiative transfer equation spatially, while spherical harmonics are used to save memory when computing scattering. SHDOM is more computationally efficient compared to Monte Carlo (MC) methods when solving the whole sky radiance field. SHDOM is also found to be within 2-3% (close to the noise level) of the MC models in the Intercomparison of 3D Radiation Codes (I3RC) (Marshak et al., 2005; Cahalan et al., 2005). Because of its computational efficiency and accuracy, SHDOM is selected for this analysis. SHDOM radiative transfer calculations are performed for 161 liquid water overcast skies with homogeneous τ_c, ranging in τ_c from 0 to 80 at solar zenith angles ranging from 21° to 70° and for wavelengths corresponding to the peaks of the USI cameras red (620 nm), green (520 nm) and blue (450 nm) channels.

Yearly average Aerosol Robotic Network (AERONET) data from the Atmospheric Radiation Measurements (ARM) Southern Great Plains (SGP) site for the year of 2013 for aerosol effective radius, and refractive index is used to calculate the single scattering properties of the aerosols in the SHDOM simulation (Holben et al. 1998; Holben et al. 2001) (Table 2.1).

Table 2.1: Atmospheric radiative properties for the ARM site used as input to SHDOM. τ_a and Rayleigh optical depth are averages for the year 2013 from AERONET data.

	Red (620 nm)	Green (520 nm)	Blue (450 nm)
τ_a [-]	0.0784	0.1010	0.1212
Rayleigh optical depth [-]	0.0875	0.1627	0.2296
Aerosol Effective Radius(R_e) [m]	3.9	3.9	3.9
Aerosol R_e distribution	Lognormal	Lognormal	Lognormal
Refractive index [-]	1.42 -0.002i	1.41 -0.002i	1.40 -0.002i

Background Rayleigh and aerosol optical depths are also obtained from yearly averages taken from the sun-tracking photometer at the ARM SGP site. Spectral surface reflectances of 0.043, 0.068, and 0.071 were used for the blue, green and red channel simulations, respectively (Marchand et al. 2004). A cloud droplet effective radius of 8 m (Min et al., 2003) is used to obtain the single scattering properties of the clouds in the SHDOM simulations. Given the desired τ_c, cloud liquid water content (LWC) for input to SHDOM is computed as (Stephens et al. 1978),

$$LWC \approx \frac{2}{3}\frac{\tau_c \rho_l r_e}{\Delta z}, \tag{2.1}$$

where ρ_l is the density of liquid water and Δz is the cloud geometric thickness. In this study, LWC is assumed constant between a cloud base of 1 km and cloud top of 2 km, giving a Δz of 1 km.

The SHDOM output radiance field is used to reproduce a sky image that would be obtained through a fisheye lens with an equisolid angle projection (Miyamoto et al., 1964),

$$r' = 2fsin(\frac{PZA}{2}), \tag{2.2}$$

where f is the focal length, and r is the distance from the principal point in the image plane.

2.2 USI hardware and calibration of the signal to radiance

On March 14, 2013 we deployed two USIs (serial numbers 1.7 and 1.8) at the ARM SGP site. The instrument domes were cleaned weekly. Daytime images from the USIs were collected continuously every 30 sec for 220 days. Since USI 1.8 was located closer (at 200 m distance) to the instruments used for validation, it is used for the analysis. The optical setup included a Sigma 4.5 mm fisheye lens, an IR filter, and an Allied Vision GE2040 CCD camera (Fig. 1.2). The fisheye lens creates an equisolid angle projection onto the CCD resulting in an image where the solid angle subtended on each CCD cell (pixel) is approximately constant. Custom apertures were inserted into the lens of both USIs with diameters of 700 m and 1000 m for USI 1.7 and 1.8, respectively. A Bayer color filter on the CCD separates pixels into red, green and blue pixels allowing for multispectral images. Three different images are taken at different exposure times and combined to create a high dynamic range (HDR) image (Urquhart et al., 2015). The signal measured by each pixel is related to the amount of photons that are transmitted through the optics and converted to a voltage. The signal measured can therefore be calibrated to estimate the irradiance, $E_{\Delta\lambda}$ at a wavelength band, incident on a pixel. The radiance $I_{\Delta\lambda}^{meas}$ observed by each pixel can then be calculated using

$$I_{\Delta\lambda}^{meas} = \frac{E_{\Delta\lambda}}{\Delta\Omega\Delta\lambda} = \frac{C_{1\lambda} * v}{\Delta t A_{in} \Delta\Omega\Delta\lambda} = C_{2\lambda * v}, \tag{2.3}$$

where v is the camera measurement in counts at a given pixel, $C_{1\lambda}$ (units of J / count) is a calibration factor between v and $E_{\Delta\lambda}$, $C_{2\lambda}$ (units of $Wm^{-2}st^{-1}nm^{-1}$) is a calibration factor between v and $I_{\Delta\lambda}^{meas}$, A_{in} is the area of the pixel, $\Delta\Omega$ is the solid angle, and $\Delta\lambda$ is the wavelength band. Given the equisolid angle lens, A_{in}, $\Delta\Omega$, and $\Delta\lambda$ are constant across the image sensor, resulting in a linear relationship (ignoring optical errors, and camera sensor nonlinearities) between the camera signal v and the radiance $I_{\Delta\lambda}$ at the PZA as

$$C_{2\lambda} = \overline{\frac{I_{\Delta\lambda}(PZA, SPA)}{v(PZA, SPA)}}. \tag{2.4}$$

The calibration constant $C_{2\lambda}$ is obtained as the average (denoted as overbar in Eq. 2.4) of 131 overcast (cloud fraction (CF) is greater than 0.9) images on 98 different days. Overcast skies are preferred because the radiance is more homogeneous and since the method by Min et al. (2003) could be applied to obtain the τ_c that is input to SHDOM. $C_{2\lambda}$ values are 1.16 x 10-4 , 1.11 x 10-4 , and 9.69 x 10-5 $Wm^{-2}st^{-1}nm^{-1}$ for the red, green and blue channels, respectively. Fig. 2.1 demonstrates the three signal calibrations with a relative root mean square error (RMSE) of 0.155, 0.148, and 0.144 for the red, green and blue channel respectively. This RMSE is within the range of the radiance variability expected in overcast clouds Szczodrak et al. (2001). Field calibration to modeled SHDOM data was preferred here as lab calibrations of sky imagers are rarely available. Therefore the calibration method presented here is more widely applicable and provides a calibration that is consistent with the Min et al. method. Validation of the field calibration with independent lab calibration is left for future work.

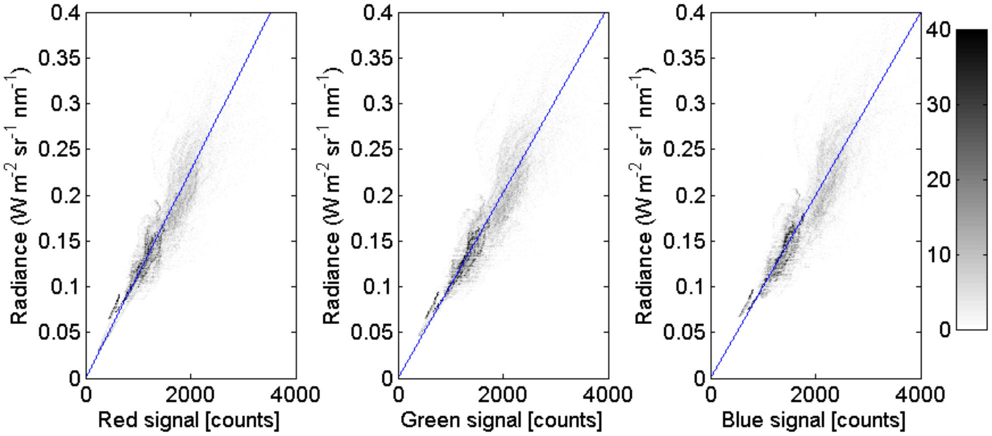

Figure 2.1: SHDOM radiance ($I_{\Delta\lambda}(PZA,SPA)$ versus USI pixel signal value (v(PZA,SPA)). Dots with greyscale indicate density while the blue line is the best fit line.

Other ground based sky imaging designs have also been developed (Seiz et al., 2007; Souza-Echer et al., 2006; Calbo et al., 2008; Cazorla et al., 2008; Heinle et al., 2010; Roman et al., 2012; Gauchet et al., 2012) with the most dissimilar design consisting of a downward pointing camera capturing the sky from a reflection off a spherical mirror (Pfister et al., 2003; Kassianov et al. 2005; Long et al., 2006; Mantelli et al., 2010; Martinez-Chico et al., 2011). Most ground imaging devices follow a relationship between the cameras signal and radiance similar to Eq. 2.3 differing only in the wavelength region $\Delta\lambda$, calibration factors $C_{1\lambda}$, and C_2 and optical and sensor errors, with non-equisolid lens camera systems requiring $\Delta\Omega$, to be specified per pixel. Therefore the method presented here can be adapted easily to images from other sky imaging systems.

2.3 Lens and Camera Imperfections

To adjust for errors due to an imperfect lens the decrease of radiance in the radial direction (vignetting) were corrected by using measurements under a Labsphere integrating sphere (LIS). The LIS provides uniform light inside of the sphere. USI 1.7 was placed inside the LIS and images were taken. Fig. 2.2 demonstrates the vignetting effects of a different USI that was deployed at ARM. Vignetting was corrected as,

$$V_c = \frac{v_0}{v_x} V, \tag{2.5}$$

where v is the original signal, v_c is the corrected signal, v_0 is the average signal value at the center of the uniform image and v_x is the signal value of the uniform image at the pixel location being corrected. For USI1.7, $v_0 = 1645$ and v_x is the green line in Fig. 2.2.

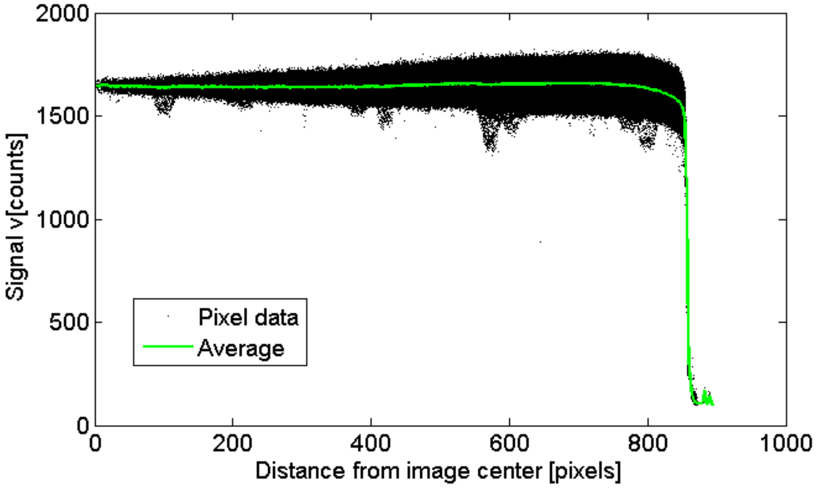

Figure 2.2: Uniformity of signal values versus pixel distance from center, taken from 12 images with USI 1.7 under a Labsphere Integrating Sphere (LIS). In the LIS pixel signal should be homogeneous.

USI 1.7 vignetting was corrected directly using the LIS. Unfortunately USI 1.8 uses a slightly different setup and USI 1.8 was not available for LIS. Instead USI 1.8 was corrected by comparing to USI 1.7 under a single overcast sky image at ARM as,

$$V_c = \frac{v_7(PZA)}{v_8(PZA)} V(PZA), \tag{2.6}$$

v_7 and v_8 are the signal of USIs 1.7 and 1.8 value under the overcast sky, respectively (Fig. 2.3).

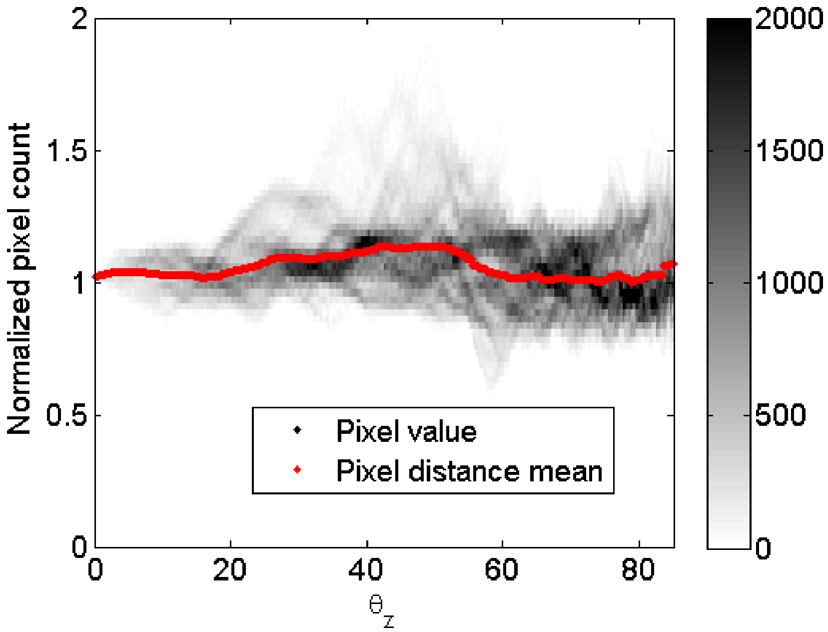

Figure 2.3: Pixel-by-pixel USI 1.7 signal for red, green and blue divided by USI 1.8 signal (v7 / v8 in Eq. 2.6) versus sky imager zenith angle for an overcast sky. The greyscale shows the number of occurrences and the red line shows the mean. Since laboratory calibrations for USI 1.8 were not available, field data from an adjacent imager that was lab-calibrated (USI 1.7) were used to reduce vignetting for USI 1.8.

2.4 Comparison of real and synthetic (SHDOM) images and stray light correction

Example measured images and their SHDOM equivalent images are illustrated in Fig. 2.4. Differences between the clear sky image (Fig. 2.4a) and the synthetic image (Fig. 2.4b) highlight the impacts of stray light as well as the vertical smear stripe caused by the CCD sensor (Fig. 2.4c). The stray light is particularly strong in the circumsolar region causing enhancement of the red radiance of up to 50%. Stray light is caused by light from the direct beam being scattered through the optics (mainly the protective acrylic dome). This means that stray light is strongest for τ_c=0 and should decrease to zero once clouds are thick enough to eliminate the direct beam which occurs at roughly $5 < \tau_c < 12$ depending on the solar zenith angle. Particular optical reflections are observed as circular patterns throughout the image that are aligned with the solar azimuth. While stray light patterns are often consistent for the same sun position, misalignments in the camera optics (e.g. during instrument maintenance) can lead to stray light changing under constant SPA, and PZA making it difficult to implement a general stray light correction, for example through a look-up table. Stray light leads to brighter pixel values than expected, which in turn can lead to misclassifications of clear sky as thin clouds (in the range $0 < \tau_c < 3$). To mitigate some of the stray light effects the SHDOM results for clear sky ($\tau_c = 0$) are replaced by the measurements from the CSL for the rest of this analysis.

Fig. 2.4d-f demonstrate USI images and a synthetic image from SHDOM for τ_c of 30. The cloud optical depth for input to SHDOM was determined from Min et al. measurements. The majority of the sky (PZA<80) red radiance differs by less than 5%. At τ_c=30 direct normal irradiance (DNI) is absent and stray light can be neglected.

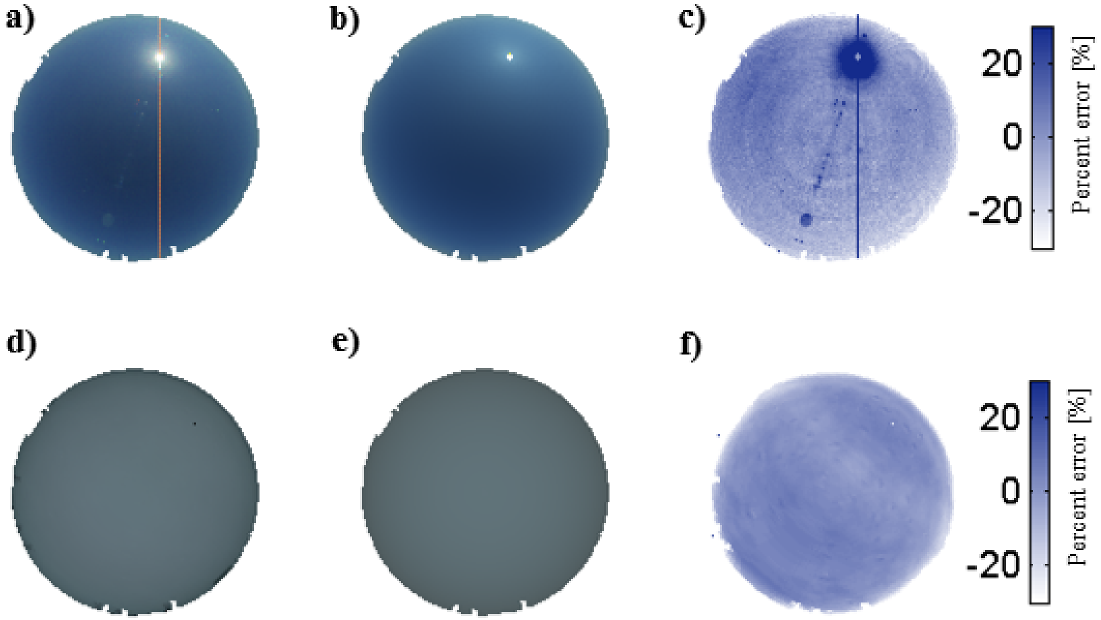

Figure 2.4: (a) Clear sky USI image for 26 March 2013, 15:00:00 UTC, (b) synthetic image from SHDOM for τ_c of 0 and SZA of 60, (c) percent error in red channel radiance, (d) USI image for 05 May 2013, 14:08:00 UTC (e) Synthetic Image for SZA of 60 and τ_c of 30, and (f) percent error in red channel radiance.

Acknowledgements

Chapter 2, in part, contains material as it appears in F. A. Mejia, B. Kurtz, K. Murray, L. M. Hinkelman, M. Sengupta, Y. Xie, and J. Kleissl, Coupling sky images with radiative transfer models: a new method to estimate cloud optical depth, Atmospheric Measurement Techniques, vol. 9, iss. 8, pp. 4151-4165, 2016. The dissertation author was the primary researcher and author of this material.

Chapter 3

Impact of geometrical parameters and cloud optical depth on radiance and RBR.

As described in chapter 1 individual channel radiance and RBR are the most fundamental parameters for cloud detection in sky images. To obtain τ_c, the functions $I_\lambda(/tau_c)$ and RBR(τ_c) must be parameterized. Furthermore, geometrical parameters (PZA, SPA), and solar position (SZA) have been found to affect RBR(τ_c) and $I_\lambda(\tau_c)$ (Shields et al.,1993) such that we must obtain RBR(τ_c,SZA,PZA,SPA) and $I_\lambda(\tau_c, SZA, PZA, SPA)$ to solve the inverse problem. With the aid of the SHDOM it is possible to analyze each of these parameters individually. In this chapter, we will discuss example cases under various SPA, PZA, and SZA to demonstrate how each variable affects I_λ and RBR.

3.1 Solar pixel angle

Fig. 3.1a demonstrates for the red and blue channel that radiance decreases with increasing SPA for non-thick clouds ($\tau_c < 30$). For thin clouds (τ_c=1) the radiance peaks in the solar region as a result of the forward scattering peak of the cloud phase function. As τ_c increases, radiance becomes constant with SPA.

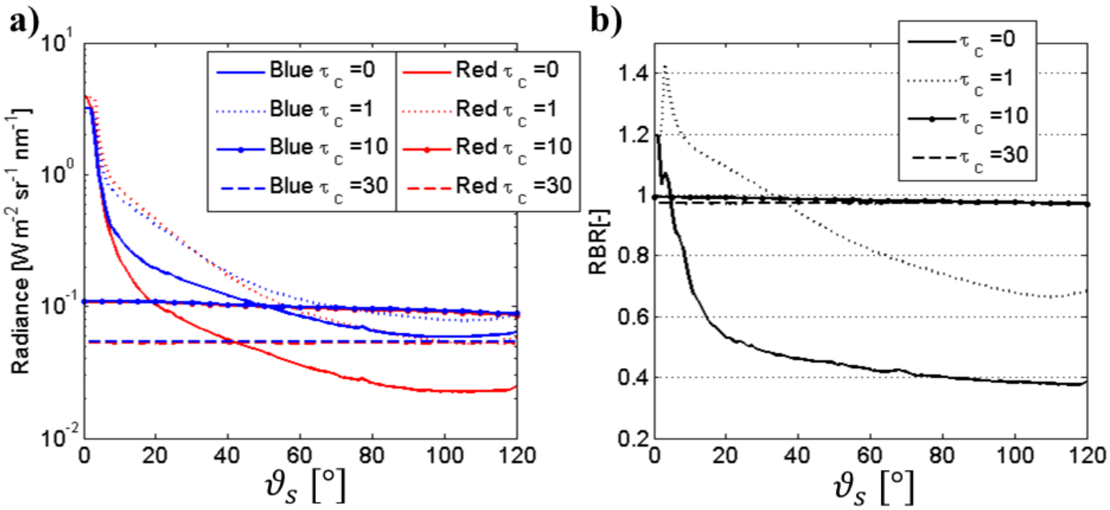

Figure 3.1: a) SHDOM red radiance over various sun pixel angles (SPA) at PZA = 60°, and SZA= 60° (Pixels used for Fig. 3.1 are highlighted as a red line in Fig. 1.3c). Results are shown for different cloud optical depths from clear (τ_c = 0) to thick clouds. b) RBR as a function of SPA at constant PZA = 60° and SPA= 60°.

Fig. 3.1a shows that the blue radiance is larger than the red radiance under clear skies, except for very small SPA, while for cloudy skies the two radiances are more similar. Therefore, most cloud detection methods assume that RBR is higher for clouds than for clear sky; however, Fig. 3.1b demonstrates that this is not always the case. At small SPA (SPA< 6°) the RBR of thick clouds is lower than that of clear sky. Moreover, as demonstrated by the τ_c=1 case thin clouds have a higher RBR at SPA< 30° than thick clouds. For τ_c <=10 RBR increases as SPA approaches the solar region. At higher τ_c (τ_c >=30) RBR becomes constant over SPA. Note that all of the statements in chapter 3 strictly only apply for the SZA and PZA shown in the figure, but Figs. 3.1-3.3 indicate that the conditions SZA= 60, SPA = 60, PZA = 60 are representative for a wide range of conditions.

3.2 Sky imager zenith angle

Near the horizon (large PZA), diffuse irradiance is commonly observed to be enhanced. Horizon brightening is indeed observed for clear skies in Fig. 3.2a. As clouds become thicker the dependence of radiance on PZA is inverted and radiance decreases with increasing PZA. The radiative transfer transitions into the diffusion regime, where it is only dependent on PZA. On the other hand the RBR dependence has a similar shape independent of the τ_c (Fig. 3.2b). Pixels near zenith have lower RBR than those near the horizon.

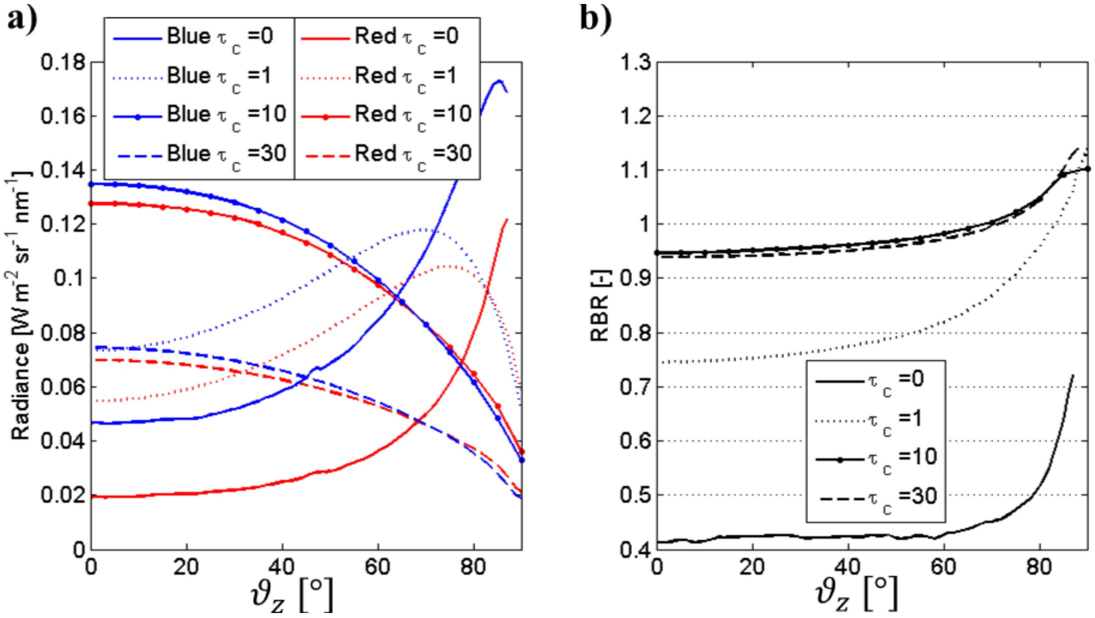

Figure 3.2: a) Red and blue channel radiances and b) RBR over various PZA at constant SPA = 60, and SZA = 60. Pixels used for Fig. 3.2 are highlighted as a red line in Fig. 1.3b.

3.3 Solar zenith angle

The effects of SZA are intuitive and consistent to what is observed during a sunset and therefore not graphically presented; the red and blue radiance is observed to decrease with increasing SZA. The decrease in radiance is caused by the decrease in extraterrestrial horizontal flux as SZA increases. On the other hand, RBR is found to increase with increasing SZA, reflecting the increase in airmass with increasing SZA. Increased airmass causes more blue light to be scattered back into space than red light.

3.4 Cloud optical depth

Fig. 3.3a illustrates the ambiguity that arises when attempting to differentiate cloud optical depth with radiance. Radiance reaches a peak at τ_c= 3.25 and almost for the entire range of τ_c there are two τ_c that lead to the same radiance. Fig. 3.3b on the other hand, demonstrates the ambiguity of τ_c detection using only RBR. SHDOM simulations demonstrate that as τ_c increases RBR increases until it reaches its maximum around τ_c= 2 and then decreases until converging to a constant value for $\tau_c >20$. This creates the following challenges: (i) RBR is insensitive to cloud τ_c for $\tau_c >20$ and therefore thick clouds of different τ_c cannot be distinguished. (ii) There is ambiguity because of the non-monotonic behavior. For example, clouds with a τ_c of 1.5 have similar RBR values to clouds of $\tau_c >20$. While (outside the solar region, see Fig. 3.1b) RBR is a useful differentiator between clouds and clear sky more information is needed to differentiate between different τ_c.

Note that while Figs. 3.3a and b demonstrate the radiance and RBR for a section of the sky these curves change throughout the sky. The dependence is illustrated for a few geometric cases through the τ_c for which the peak in the red radiance is observed. In the circumsolar region red radiance peaks at $\tau_c \sim 0.75$ while clear sky has a higher radiance than thick clouds ($\tau_c > 5$). A similar trend is observed for RBR, where clear sky has a higher RBR than thick clouds ($\tau_c > 5$). Approaching PZA=0 and on the opposite side of the sun (SPA> 60°), the red radiance peaks at τ_c=8.75. Near the horizon (PZA > 80°) the red radiance peaks again at lower τ_c=1.25.

In addition, Fig. 3.3a highlights one of the main challenges of ground based images compared to satellite based cloud detection. In satellite based τ_c detection, the measured radiance can be used to calculate τ_c (Nakajima et al., 1990) as the measured (upwelling) radiance monotonically increases with higher τ_c. This same method cannot be used for ground based imagery as radiance increases for thin clouds peaks and then begins to decrease. This means that there can exist two τ_c that produce the same radiance. It is again important to also note that the curves in Fig. 3.3 depend on SPA and PZA. For example, in the circumsolar (SPA< 30°) region red radiance peaks at $\tau_c \sim 0.75$ while clear sky has a higher radiance and higher RBR than thick clouds ($\tau_c > 5$). Approaching PZA=0 and far from the sun (SPA> 60°), the red radiance peaks at τ_c =8.75. Near the horizon (PZA> 80°) the red radiance peaks again at lower τ_c =1.25.

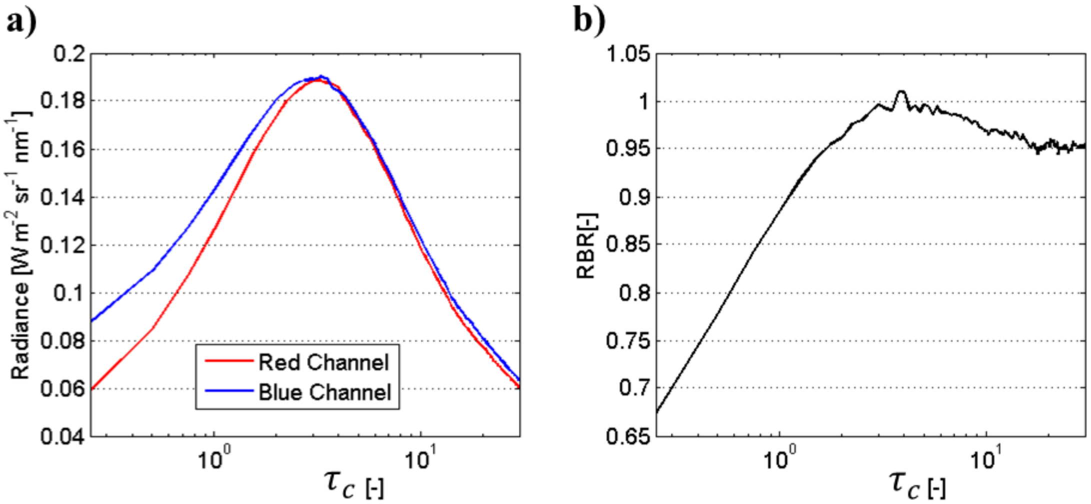

Figure 3.3: Red and blue channel blue channel radiance (a) and RBR (b) versus τ_c for SPA of 45°, SZA of 60° and PZA of 45°.

3.5 Expressing cloud optical depth through geometrical and solar parameters

Since it is currently computationally infeasible to use SHDOM to solve τ_c (I_λ,RBR,SZA,SPA,PZA) in real-time (10 sec) as required for sky imager solar forecasting, the homogeneous cases described in section 3.1 are used instead to create interpolants. As seen in Figs. 3.3a and 3.3b τ_c (I_λ,SZA,SPA,PZA) and τ_c (RBR,SZA,SPA,PZA) are multivalued functions. Therefore two separate interpolants are created for each function. τ_c (I_λ,SZA,SPA,PZA) is split into τ_c that are higher than the peak radiance and τ_c that are lower than the peak radiance. τ_c (RBR,SZA,SPA,PZA) is similarly split into τ_c that are higher than the peak RBR and τ_c that are lower than the peak RBR. Section 3.6 will describe how these interpolants are used to find up to two τ_c (I_λ^{meas}) (one for the higher and one for the lower branch of τ_c) and how a unique τ_c is obtained.

3.6 Radiance red blue ratio (RRBR) method for cloud optical depth measurement

We have shown that it is difficult to distinguish between different τ_c by using RBR alone. As demonstrated in Fig. 3.3 radiance and RBR are non-monotonic functions of τ_c with generally two τ_c associated with the same radiance or RBR. However, for most cases, there is a unique τ_c solution for a pair of RBR and radiance. The RRBR method attempts to obtain this solution by first solving τ_c (I_λ,SZA,SPA,PZA) and then substituting the (usually two) τ_c solutions into RBR(τ_c,SZA,SPA,PZA) and identifying the correct τ_c as the one with the smallest $|RBR^{meas}(SZA,SPA,PZA) - RBR(\tau_c,SZA,SPA,PZA)|$, where $RBR^{meas}(SZA,SPA,PZA)$ is the measured RBR. The algorithm for the RRBR method is depicted graphically in Fig. 3.4. I_λ at a wavelength of 620 nm is used because its variations with τ_c are larger than the other wavelengths. This larger dynamic range reduces the errors caused by instrument noise.

The algorithm begins by comparing $I_{620}^{meas}(SZA,SPA,PZA)$ against max($I_{620}(\tau_c, SZA,SPA,PZA)$) (e.g. 0.19 $Wm^{-2}st^{-1}nm^{-1}$ in Fig. 3.3a), where $I_{620}^{meas}(SZA,SPA,PZA)$ is the measured radiance in the cameras red channel. Heterogeneity in clouds can cause $I_{620}^{meas}(SZA,SPA,PZA)$ to be larger than max($I_{620}(\tau_c,SZA,SPA,PZA)$); in this case as the pixel conditions fall outside the range of the method the algorithm reverts back to τ_c assignment solely based on RBR and $\tau_c(RBR,SZA,SPA,PZA)$ is used to find τ_c. If there are two solutions, then the τ_c associated with the maximum red radiance is used as there is no way to differentiate between the multiple solutions. Clouds brighter than the SHDOM radiance peak were found to only occur in 5.4% of all pixels.

If $I_{620}^{meas}(SZA,SPA,PZA)$ is within the range of $I_{620}(\tau_c,SZA,SPA,PZA)$, then τ_c is calculated from $\tau_c(I_{620}^{meas},SZA,SPA,PZA)$. If only one solution is found the τ_c is assigned based on $\tau_c(I_{620}^{meas},SZA,SPA,PZA)$ and $RBR(\tau_c,SZA,SPA,PZA)$ is not considered. When two solutions are found, they are input into $RBR(\tau_c,SZA,SPA,PZA)$ and the one closest to $RBR^{meas}(SZA,SPA,PZA)$ is assigned.

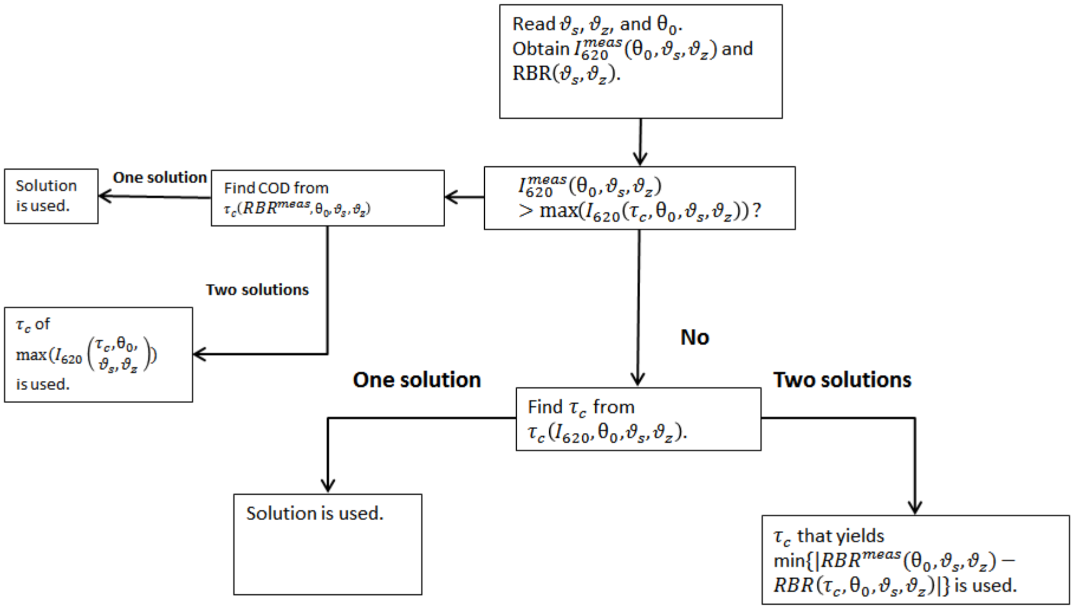

Figure 3.4: Flowchart of the radiance red blue ratio (RRBR) method for τ_c estimation. If $I_{620}^{meas}(SZA, SPA, PZA)$ is saturated (e.g. in the solar disk), τ_c is assigned Not-a-Number.

An example τ_c estimate is presented in Fig. 3.5. The darker clouds are correctly identified as higher τ_c, even though the RBR is lower than for the thinner clouds, for example for the clouds between the sun and the horizon. In the circumsolar region, the RBR is largest but the RRBR method correctly identifies a thinner cloud. The black points in Fig. 3.5b corresponds to undetermined τ_c due to signal saturation. Since saturated pixel values near the sun exceed the dynamic range of the USI sensor, the RBR defaults to 1, the red radiance is unknown, and no τ_c can be assigned. In practice one could interpolate across the saturated region, but we prefer showing the raw results in this paper.

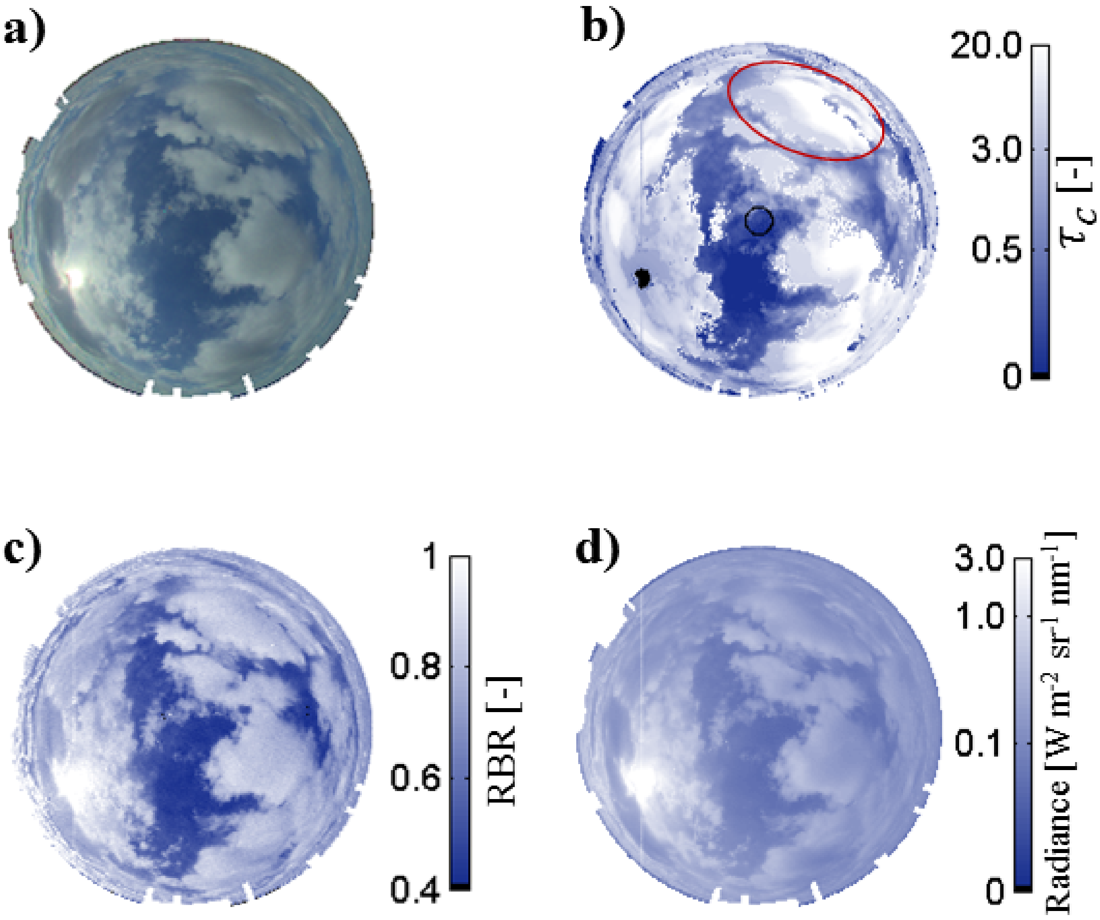

Figure 3.5: (a) USI image for 25 March 2013, 22:10:00 UTC. (b) τ_c retrieval from the RRBR method. Pixels inside the black ring are the pixels used for averaging and comparison with the MWR (Section 6.4) (c) $RBR^{meas}(SPA,PZA)$. (d) $I_{620}^{meas}(SZA,SPA,PZA)$. For this scene, the MWR measured a τ_c of 0.56 and the USI measured a τ_c of 0.20, the highest τ_c readings within 10 minutes of this image are 19.4 and 15.3 for the MWR and USI respectively.

3.7 Impact of 3-D effects

Although the RRBR method is developed from overcast scenarios, we also apply this method to broken cloud scenes. The largest 3-D effect is the geometric difference in a broken clouds optical path (τ_p) compared to an overcast clouds τ_p (Hinkelman et al., 2007). Fig. 3.6 illustrates the definition of τ_p as the optical thickness along the path of the direct solar beam, while τ_c is the optical thickness integrated along the vertical direction. For overcast clouds the τ_p is simply related to the τ_c as,

$$\tau_c = \tau_p cos(SZA). \tag{3.1}$$

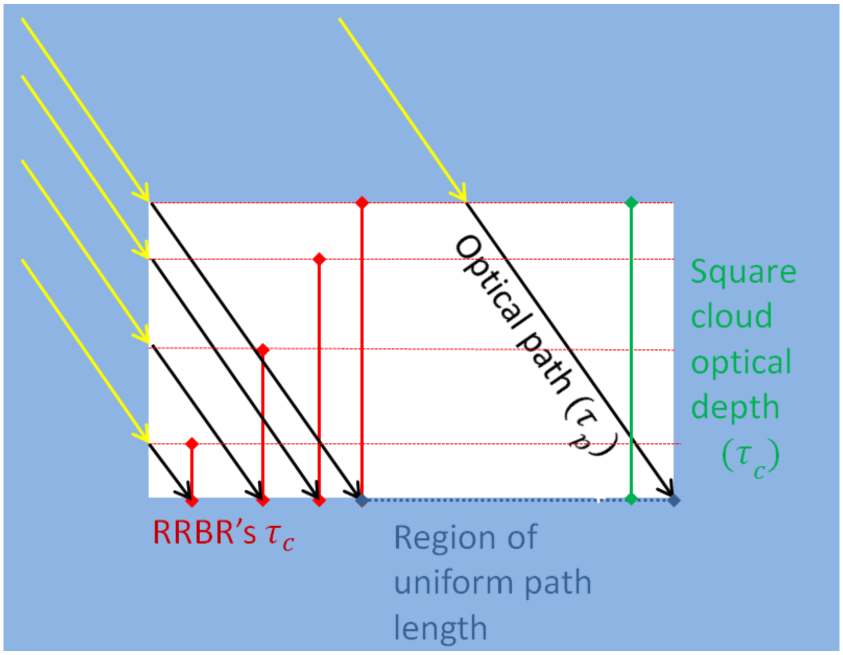

Figure 3.6: Illustration demonstrating differences between RRBR measured cloud optical depth, cloud optical depth and cloud optical path.

But for partial cloud cover the optical path changes along the cloud and as a result it affects I_λ, which in turn affects the RRBR retrieval. Ignoring horizontal photon transport, the RRBRs τ_c is then a function of the τ_p as in equation 3.1, which unlike the actual τ_c changes across the square cloud. Fig. 3.7 demonstrates how the RRBR method retrieves τ_c for a 1 km x 1 km square cloud with a 0.2 km cloud geometric thickness. τ_c is observed to increase in the same way that τ_p increases. Therefore differences between the actual τ_c and the RRBRs τ_c will occur based on the geometry of the cloud. Again ignoring horizontal photon transport, in ideal cases, such as a cubic cloud, the region of uniform path length where the actual τ_c and the RRBRs τ_c are similar are limited to

SZA<<45 °. For square clouds with a small vertical extent, the region of uniform path length is increased while for a square cloud of large vertical extent the region of uniform path length is decreased compared to the cubic cloud. For a parallelogram cloud aligned with the solar beam, the local homogeneity is extended to include most of the cloud base. The specifics of defining when clouds can be considered locally homogeneous will be left for future work. When horizontal photon transport is included it would be expected to decrease the area of homogeneity.

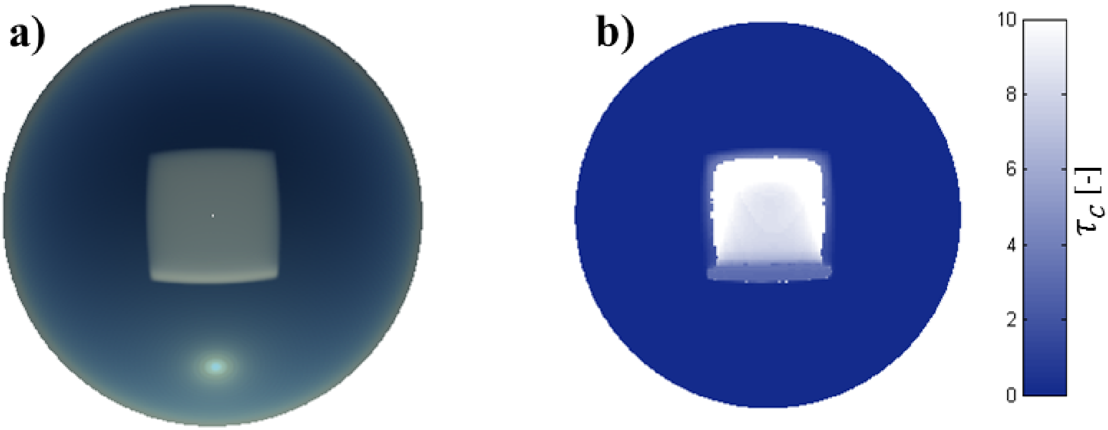

Figure 3.7: (a) SHDOM simulated sky image of a 1km x 1km square cloud with cloud geometric thickness of 0.2 km at a SZA=60° and τ_c =10 (b) and RRBR τ_c retrieval. The RRBR τ_c is 8 0.2 km from the cloud edge facing the sun.

The second major 3-D effect is that heterogeneous clouds are brighter than homogeneous clouds under the same τ_c. This is caused by increased upwelling solar irradiance from the unshaded part of the scene illuminating the cloud from below. The reflected light from the cloud underside increases brightness. This is demonstrated in Fig. 3.8 where overcast and square clouds where compared for two different spectral surface reflectance (R) for τ_c=10. The results demonstrate that the cloud bottom radiance increases 5% due to a spectral surface reflectance of 0.08 at a wavelength of 620 nm. Adjusting the RRBR method to account for these effects is left for future work.

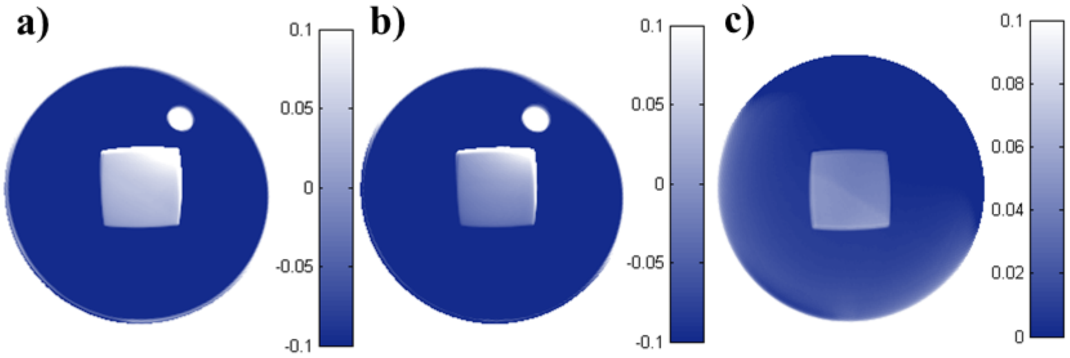

Figure 3.8: Relative difference in red radiance [-] between square and overcast clouds, (a) for surface reflectance R = 0.08 and (b) R =0 (c) difference between (a) and (b).

3.8 Impact of aerosols

The chosen τ_a is an additional source of error in the reference SHDOM simulations. Higher actual τ_a values than those in the simulations may lead to τ_a being classified as τ_c , while smaller τ_a lead to a reduced τ_c estimate. This error is small since most τ_c are much larger than the variations in τ_a in the US. Furthermore, this error is not important for solar forecasting as spectral effects aside only the total atmospheric optical depth is of interest to estimate ground irradiance, not the partition between τ_a and τ_c . As demonstrated in Fig. 3.9 variations in AOD from 0 to 0.2 lead to changes in I_λ and RBR of less than 5%.

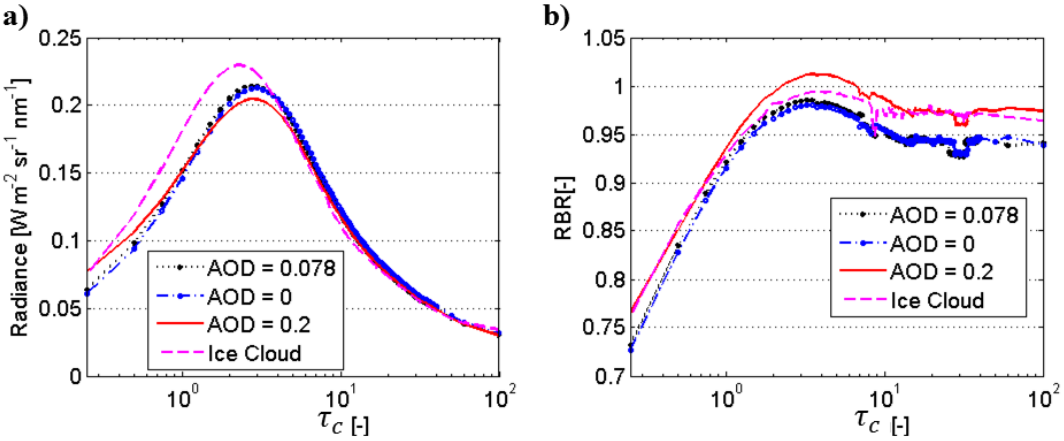

Figure 3.9: (a) Red radiance and (b) RBR for liquid clouds with τ_a= 0, 0.078, and 0.2, and ice clouds with τ_a= 0.078 versus τ_c for SPA= 45°, SZA= 60° and PZA= 45°.

The RRBR method was derived based on SHDOM results for a single layer liquid clouds but the model could be extended to ice clouds with additional SHDOM runs. Fig. 3.9 demonstrates results from ice cloud simulations, with an effective radius of 100 m. Ice clouds are not assessed in this paper as none of the methods used for validation provide information for ice clouds. As for cloud scenes with multiple layers, the RRBR method represents the additive τ_c of all cloud layers.

3.9 Cloud optical depth measurements for validation

The Min et al. method (Min and Harrison. 1996b; Min et al. 2003) is designed to estimate τ_c for conditions with homogenous clouds using the measured atmospheric transmittance of global radiation (also referred to as clearness index). The atmospheric transmittance is obtained using a multifilter rotating shadowband radiometer (MFRSR) as,

$$T = \frac{GHI^{415nm}}{GHI_0^{415nm}}, \tag{3.2}$$

where GHI^{415nm} is the global horizontal irradiance, and GHI_0^{415nm} is the top of the atmosphere GHI, both at a wavelength of 415 nm. The MFRSR measurements at a wavelength of 415 nm is used in Eq. 3.2 to reduce effects of gaseous absorption. GHI_0 is adjusted from the true TOA GHI to remove τ_a influences on T, by applying Langley regression calibrations from the direct normal irradiance (DNI) on clear skies to the GHI (Harrison et al. 1994; Min et al. 1996b). A discrete ordinate radiative transfer model is applied to identify the τ_c corresponding to the measured T (Min et al. 1996a). By default a cloud effective radius (r_e) of 8 μm is assumed in the Min et al. method, but when liquid water path (LWP) values are available from a microwave radiometer (MWR), then r_e is solved iteratively. r_e is first solved for with Eq. 3.3 using LWP from the MWR and the Min et al. τ_c . Once its obtained it is used as an input in the discrete ordinate model, which provides a different τ_c , which leads to a different r_e , and this process is repeated until the changes in τ_c are below a threshold value. Min et al. concluded that the uncertainty in the inferred cloud properties caused by r_e was less than 5%. Since the Min et al. method uses GHI measurements to estimate τ_c , the τ_c is representative of the sky hemisphere. At the ARM site the Min et al. τ_c is sampled and reported every 20 sec. Since the Min et al. method only works for liquid clouds only data with cloud height less than 9 km as observed from a ceilometer was used. Accurate τ_c are obtained with this method for $\tau_c > 10$ but for $\tau_c < 10$ the Min method is no longer valid (Turner et al., 2004.) τ_c is also measured by a MWR. The MWR is a microwave receiver that detects the microwave emissions of the vapor and liquid water molecules. It measures cloud liquid water path (LWP) in the zenith direction within a field of view of 6° (Liljegren et al. 2000; Cadeddu et al. 2013). τ_c can then be estimated as (Stephens et al. 1978)

$$\tau_c \approx \frac{\frac{3}{2}\int LWCdz}{\rho_l r_e} = \frac{3/2LWP}{\rho_l r_e}) \tag{3.3}$$

where LWC is the cloud liquid water content and ρ_l is the density of liquid water. A r_e of 8 μm is assumed, as in the Min et al. method. The MWR has an irregular timestep ranging from 20 to 40 sec. The uncertainty in the LWP obtained from the MWR is ± 0.03 mm (30 g m^{-2}, Morris et al., 2006) which corresponds to a τ_c of ± 5.6 with Eq. 8.

3.10 Comparison in overcast conditions with Min algorithm

Data from the Min et al. algorithm is compared to the average τ_c from an entire USI image. Since the Min et al. method assumes overcast skies, only conditions with cloud fraction (CF)>0.7 are used for this analysis yielding 5197 datapoints (about 43 hours of data). The mean transmission of horizontally heterogeneous clouds is higher than the transmission of a uniform cloud with the same mean optical depth (Hinkelman et al., 2007). This is caused by the nonlinear relationship between τ_c and radiance.

To adjust the heterogeneous USI τ_c retrieval to be consistent with the Min et al. method, the USI τ_c was converted to irradiance for each pixel using a look up table, averaged over the entire image in irradiance space, and then converted back to τ_c. The look up table was developed from the homogeneous library of images. Fig. 3.10 compares results from both methods. An R^2 of 0.99 reflects the high correlation between the two methods. The relative RMSE decreases as τ_c increases as demonstrated in Table 3.1, with thin clouds (τ_c <10) having an RMSE of 27.2% and thick clouds (τ_c >30) having an RMSE of 5.8% with the overall RMSE being 8.2%. RMSE at τ_c >10 is well below the 21% required for solar energy applications (Fig. 1.1) and validates the RRBR method for thick overcast clouds (τ_c >10), but for τ_c <10 the Min et al. method is no longer valid (Turner et al., 2004) and the relative RMSE increases drastically. These differences in RMSE between τ_c highlight the difficulties in detecting thin clouds correctly.

Note that the zero MBE between Min and RRBR for CF $>$ 0.7 is partially a result of the cross-calibration in overcast conditions (since the cross-calibration data required CF $>$ 0.95 the cross-calibration and validation data are different). However, the other errors between Min and RRBR in Table 3.1 are non-zero because (i) some of the data used for the comparison was not used for radiometric calibration, (ii) differences in the wavelengths of measurement (620 nm for RRBR and 450 nm for USI), (iii) radiation differences as USI uses diffuse radiance while Min uses global irradiance to derive τ_c. Nevertheless the cross-calibration is expected to reduce the mean bias difference between Min and RRBR methods and the related error metrics are not representative of a truly independent dataset especially for the CF $>$ 0.7 scenario.

Table 3.1: Statistics of RRBR comparison against the Min et al. method in overcast skies (cloud fraction $>$ 0.7), and microwave radiometer (MWR) measurements. RMSE[-] is the absolute root mean square error, RMSE[%] is the relative root mean square error, MAE[%] is the relative mean average error, and MBE[%] is the relative mean bias error.

Method	CF	τ_c	R2	RMSE [-]	RMSE [%]	MAE [%]	MBE [%]
Min	$>$ 0.7	All	0.99	2.5	8.2	6.1	0.0
Min	$>$ 0.7	$<$ 10	0.55	1.6	27.2	20.6	12.1
Min	$>$ 0.7	$>$ 10 & $<$ 30	0.88	1.8	9.3	7.2	-1.2
Min	$>$ 0.7	$>$ 30	0.97	3.4	5.8	4.5	-1.0
MWR	All	All	0.98	3.6	19.0	11.3	1.1
MWR	$>$ 0.7	All	0.97	4.3	14.3	9.3	2.1
MWR	$<$ 0.7	All	0.68	2.2	85.0	46.6	-14.4
MWR	$<$ 0.7	$<$ 10	0.58	1.5	71.7	49.9	-11.3
MWR	$<$ 0.7	$>$ 10 & $<$ 30	0.42	4.5	31.9	24.6	-16.7
MWR	$<$ 0.7	$>$ 30	0.50	24.8	56.8	52.8	-52.8

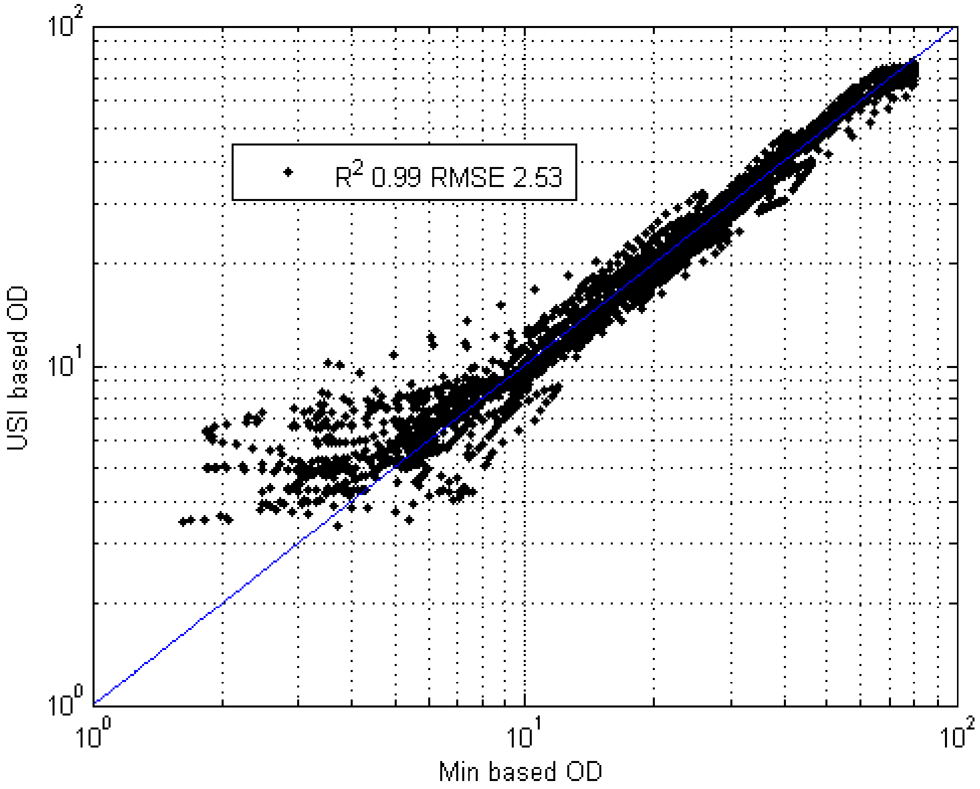

Figure 3.10: Comparison of RRBR τ_c retrievals from the sky imager versus the Min et al. method applied to MFRSR measurements for USI cloud fractions greater than 0.7.

3.11 Heterogeneous and homogenous cloud conditions with the microwave radiometer

The RRBR method is compared to τ_c estimates from the microwave radiometer (MWR) using the 12,422 pixels in each USI image with PZA$<6°$. Fig. 3.11 shows the comparison of the two methods. Overcast conditions result in a RMSE of 3.6 or 19.0% and R2 of 0.98 again well within the minimum error requirement of 21%. Since overcast data were already validated in Section 3.10 we now focus on cloud fractions of less than 0.7.

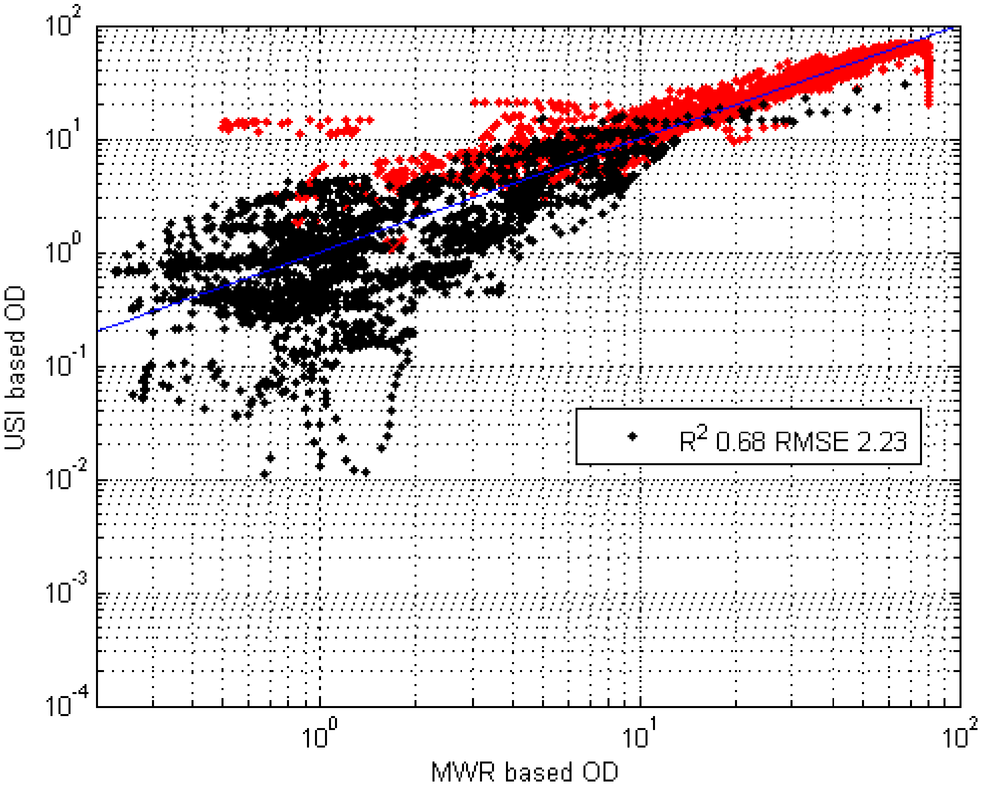

Figure 3.11: Comparison of USI RRBR versus MWR measurements of cloud optical depth for CF<0.7 in black and CF> 0.7 in red.

The RMSE is 2.23 for the heterogeneous cases, which is well within the uncertainty of the MWR measurements of ± 5.6 but that corresponds to a relative RMSE of 85.0% that exceeds the objectives set at the beginning. Just like in overcast conditions (section 6.2), RMSE is highest for thin clouds ($\tau_c < 5$) at 71.7%, decreases at medium cloud thickness ($10 < \tau_c < 30$) to 31.9%, and increases once again for thick clouds ($\tau_c > 30$) to an RMSE of 56.8%. The heterogeneous cases are associated with a higher relative RMSE of 85.0% compared to 8.2% reported in section 3.10 for the homogeneous Min et al. method. The lower correlation of 0.66 between the two methods is probably related (i) the uncertainty of the MWR, and (ii) random errors in τ_c retrievals under heterogeneous cloud conditions due to incomplete overlap of the field-of-view of the USI and MWR,

(iii) 3-D cloud effects (Section 3.7) and (iv) uncertainty in the MWR τ_c related to the assumption of $r_e = 8\ \mu m$. While the SHDOM model calculations also assume constant r_e , this only affects the single scattering properties of the cloud, more specifically the phase function. Consequently, the MWR algorithm is more sensitive to r_e as r_e errors are linearly proportional to MWR errors.

A mean bias error (MBE) of -14.4% is observed demonstrating a tendency for the RRBR method to under predict τ_c . This can further be analyzed when MBE is split into τ_c categories. Thick clouds ($\tau_c > 30$) have the highest MBE of -52.8% compared to thin clouds ($\tau_c < 10$) that have an MBE of -11.3%. As described in section 3.7 heterogeneous clouds are brighter than homogeneous clouds because of the reflected light from the ground surface, leading to higher radiance measurements and lower τ_c . Another factor that causes higher USI radiance measurements in heterogeneous clouds are cloud sides. Since clouds sides are no longer obscured such as those in overcast clouds, an increase in cloud illumination relative to overcast clouds increases radiance. For clouds that are thicker than the red radiance peak ($\tau_c = 7.25$) this increased radiance along the sun-facing edge of the cloud results in an under prediction of τ_c. The fact that MBE become more negative with increasing τ_c could be a result of neglecting 3D effects in the RRBR method.

Acknowledgements

Chapter 3, in part, contains material as it appears in F. A. Mejia, B. Kurtz, K. Murray, L. M. Hinkelman, M. Sengupta, Y. Xie, and J. Kleissl, Coupling sky images with radiative transfer models: a new method to estimate cloud optical depth, Atmospheric Measurement Techniques, vol. 9, iss. 8, pp. 4151-4165, 2016. The dissertation author was the primary researcher and author of this material.

Chapter 4

Cloud tomography applied to sky images: Part I: A virtual testbed

4.1 Basic Principle

Using the results from 3.6 we can now estimate τ_c, as such we can use this estimate to solve the 3-D cloud problem. To solve for this 3-D cloud scene, we need to know the k, at any point in the cloud scene. Similar problems exist in medical imaging, archaeology, and, generally, remote sensing. The measurements used for tomographic reconstruction are based on the measurements of line integrals. For medical imaging of tissue, these are measurements of attenuated radiation as

$$I = I_0 e^{-\int k(x,y,z)ds} \tag{4.1}$$

where I_0 is the emitted radiation and s is the path along the beam. By taking several measurements of I from different perspectives, k can be solved. Computed tomography (CT) scans achieves this by using an inverse radon transform to convert I measurements into *k*. For our application, we need to find the unknown *k* of clouds from measurements of I by multiple sky imagers. The following two methods are applied to multiple camera images.

4.2 Algebraic Reconstruction Technique

In the atmospheric sciences, tomographic techniques for cloud reconstruction have focused on MWR measurements of the line integrals of cloud emission from various azimuth and zenith directions (PAA,PZA). The cloud domain is discretized and a system of linear equations is set up to relate *k* and MWR measurement *I* (Huang et al. 2008). *k* is obtained by solving the system of linear equations. For SIs, we obtain τ_i estimates from the radiance red-blue ratio (RRBR) method (Mejia et al. 2016), were i is the pixel index. The RRBR method uses a look up table method of homogenous clouds to estimate τ_i and, therefore, we calculate k such that the sum of *k* is τ_i. τ_i is then a vector of individual scalar τ_i from each pixel in a sky image, defined at pixel zenith angles (PZA, or view angle) and azimuthal angles (PAA). *k* is a vector of all extinction coefficients in the domain with corresponding *x, y, z* coordinate. *A* system of linear equations between *k* and τ_c is then,

$$Ak = \tau_i. \tag{4.2}$$

We approximate line integrals by assuming that only one grid cell contributes at each *z* level, such that *A* is a matrix with ones when the element a_{im} satisfies the following equalities:

$$x_{im} = nearest(z_i tan(PZA) sin(PAA) + x_{si}) \tag{4.3}$$

$$y_{im} = nearest(z_i tan(PZA) cos(PAA) + y_{si}) \tag{4.4}$$

and zero everywhere else. i is the pixel index and $m = 1, ..., N_m$ is the domain point index that covers all points where k is defined in the $N_m = N_x N_y N_z$ 3D carthesian domain. x_{si} and y_{si} are the coordinates of the SIs. Nearest represents rounding to the nearest grid point. This provides a sparse matrix reducing the computational cost of solving the system of equations. An example of these equalities is demonstrated in Fig. 4.1.

To solve this system of equations, we will use the ART of Gordon et al. (1970). ART is a family of algorithms used to reconstruct a domain *k* by solving a system of linear equations. The conventional ART method iteratively adjusts *k* as,

$$k_j = k_{j-1} + (\frac{\tau_n - a_n k}{||a_n^2||} a_n) \tag{4.5}$$

where a_n is the n-th row of the matrix A, which corresponds to the relation between one pixel in an image and the entire atmospheric domain (i.e. all *k* in 3-D), τ_n is the n-th element of τ_c, and j is the iterative step. Our implementation slightly differs by iteratively adjusting *k* as,

$$k_j = k_{j-1}(1 + (w(\frac{\tau_n}{a_n k} - 1) \tag{4.6}$$

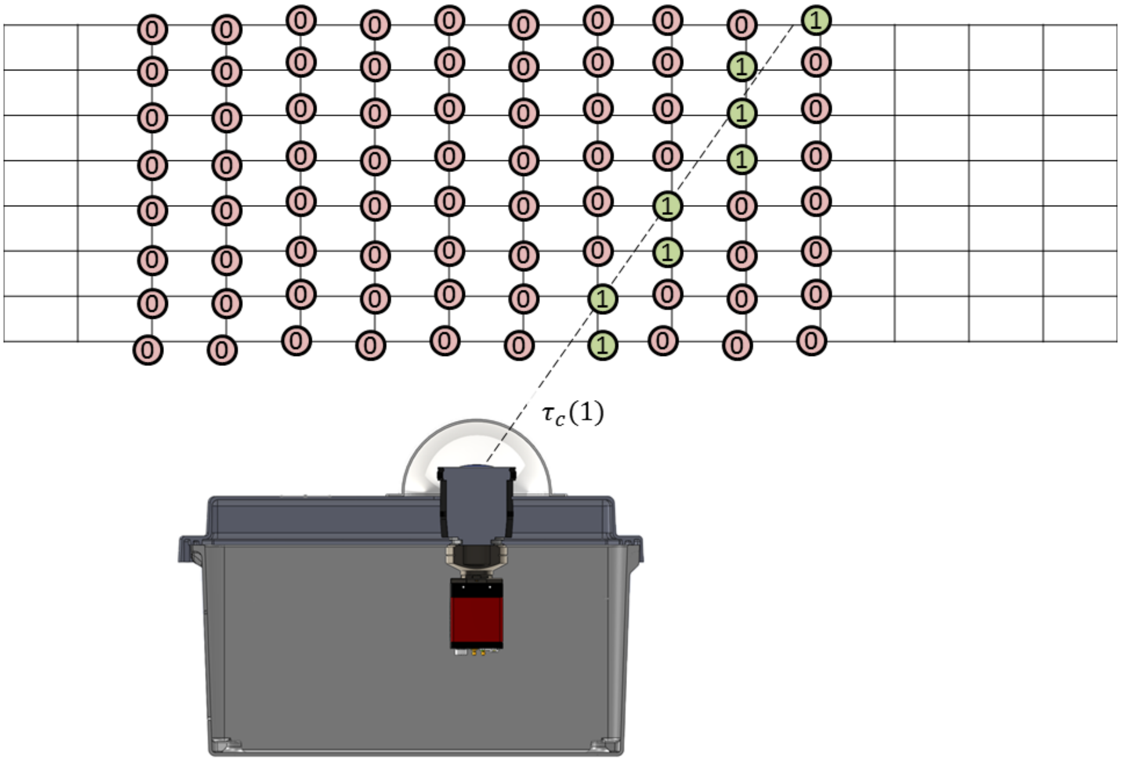

Figure 4.1: Conceptual diagram of ray tracing to create matrix A in Eq. 4.2 for one SI pixel.

where w is a weighting term set to 0.2. Eq. 4.6 is preferred over Eq. 4.5 as it naturally limits k to only positive values as opposed to the original ART method. The solutions k_j are further constrained by requiring k_j=0 when τ_n=0. k_j are only updated (applying Eq. 4.6) for the corresponding non-zero elements of a_n, i.e. for cloudy pixels.

4.3 Iterative Retrieval

Another approach developed by Levis et al. (2015) is to iteratively simulate the line integral I through a radiative transfer model and apply a gradient descent to the difference between measured and simulated I. To solve for k in 3-D, we will iteratively run SHDOM simulations to minimize the error, $I^{meas} - I$ for each pixel in an image. The dependence of $I^{meas} - I$ on k is described by the integral form of the radiative transfer equation,

$$I(s,\omega) = e^{-\int_0^s k(s')ds} I(s_0,\omega) + \int_0^s e^{-\int_{s'}^s k(t)dt} J(s',\omega) k(s') ds' \tag{4.7}$$

where $I(s_0,\omega)$ is extraterrestrial radiance, s is the position vector along the view path (i.e. line integral) illustrated as the dashed line in Fig. 4.1, ω is the unit vector representing the angular direction of the view path, t is a dummy variable for integration and J is the source function. Neglecting emission from the cloud, the source function J is,

$$J(s,\omega) = \frac{\overline{w}}{4\pi} \int_0^{4\pi} I(s,\omega') P(s;\omega,\omega') d\omega' \tag{4.8}$$

where P is the phase function, and $\overline{w}$ is the single scattering albedo. Eq. 4.7 shows that I explicitly depends on the local k through the integral along the view path. When discretized, this means that I depends on the k located along that I view path as illustrated in Fig. 4.1. This integral of k in Eq. 4.7 is easily iterated to minimize $I^{meas} - I$ (described in Eq. 4.9 below), but J causes the iterative process for one direction to depend on the iterations at all other angles through 3-D scattering effects. As demonstrated in Eq. 4.7 and 4.8, I also implicitly depends on k through J because scattering anywhere in the domain can increase J at a particular view path. J depends on the I in all directions such that iterating neighboring pixels affect all other pixels. To solve this problem, Levis et al. did not update J in the iterative process and instead J from a first guess k simulation was input to Eq. 4.7, leaving I^{meas} only a function of local k through the view path integral. Fig. 4.2 demonstrates the flow chart of the implementation of this iterative process.

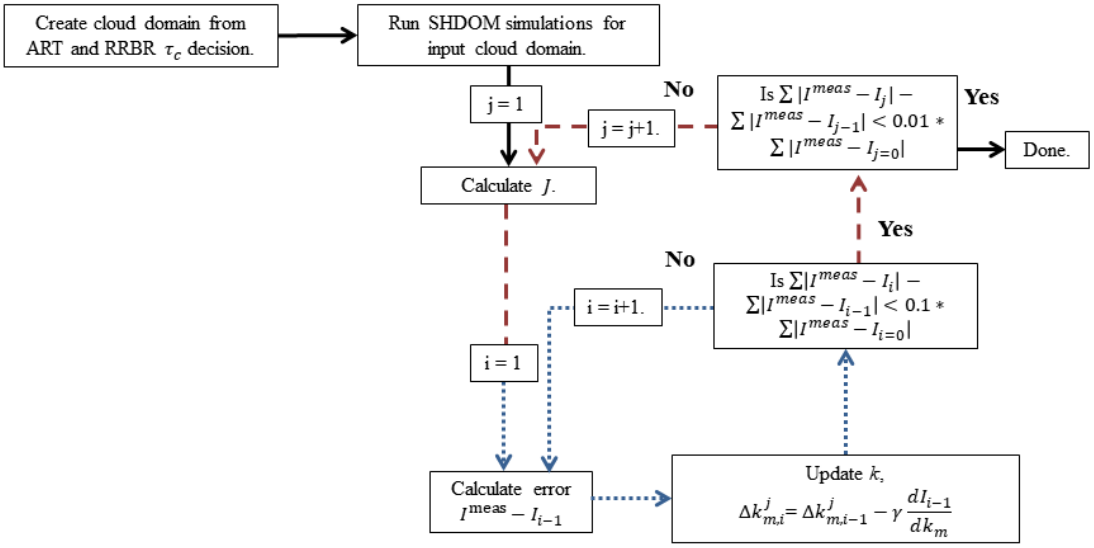

Figure 4.2: Flow chart of the iterative retrieval method. Dashed, dotted and dashed dotted arrows correspond to pixel, constant source function and constant pixel iterations respectively.

Therefore, the iterative process to minimize $I^{meas} - I$ consists of adjusting k at grid point m following a gradient descent method as

$$k^j_{m,i} = k^j_{m,i-1} - \gamma \frac{dI_{i-1}}{dk_m}, \tag{4.9}$$

where j is the constant source function iterative step, i is the gradient descent iterative step, and γ is the step size. Each iterative step considers a different pixel I_i until convergence is met when the change in the total image error is less than 1% of the original error as,

$$\sum |I^{meas} - I_i| - \sum |I^{meas} - I_{i-1}| < 0.01 * \sum |I^{meas} - I_{i=0}|, \tag{4.10}$$

where $\sum$ represents summation over all pixels in all images.Once this convergence criterion is met the J is recalculated until the change in the total image error decreases to 1% of the original error as,

$$\sum|I^{meas} - I_j| - \sum|I^{meas} - I_{j-1}| < 0.01 * \sum|I^{meas} - I_{j=0}|, \tag{4.11}$$

4.4 Constraining Cloud Base and Cloud Top Height

Fig. 4.3 demonstrates one of the clouds scenes with a cloud top height (CTH) of 1.2 km and a cloud base height (CBH) of 820m. As seen in Fig. 4.3, cloud artifacts are erroneously reconstructed below and above the real cloud layer. In general, this is because Eq. 4.2 is ill-conditioned. For clouds at low heights or closely spaced imagers (i.e. small CBH / l), this is because of a lack of different perspectives for those low level points. To remove these artifacts, we will assume that no clouds are present 250 m below the CBH or 250 m above the cloud top height (CTH). For this simulated case, the CBH and CTH are the heights of the highest and lowest non-zero k_{LES}, respectively. k_{LES} are the extinction coefficients calculated from the LES results. The height restriction could also be applied in practice. For example, ceilometer data is used to determine the CBH within 250 m accuracy. Estimating CTH is more challenging, but CTH could be estimated with temperature and humidity profiles from radiosoundings.

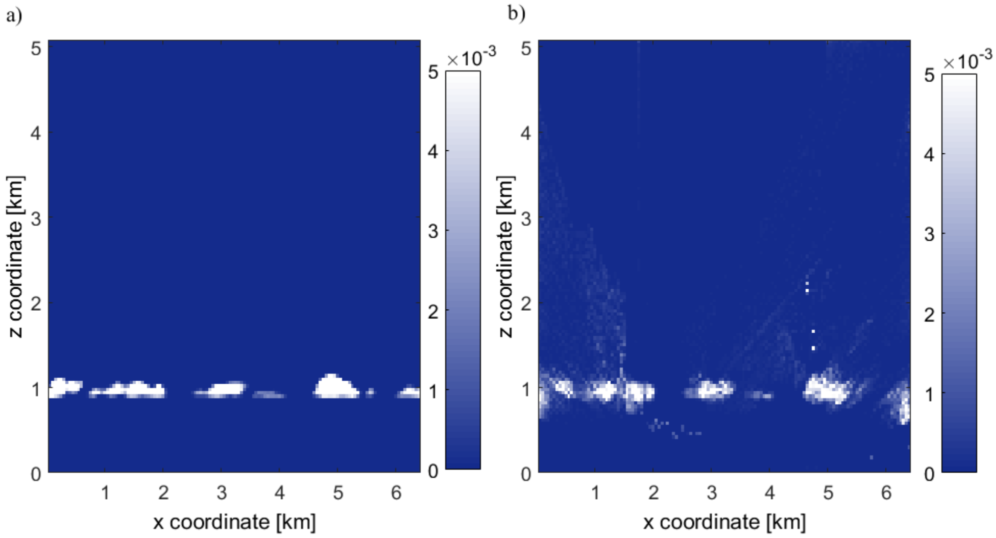

Figure 4.3: 2-D slice through *k* from Large Eddy Simulation (LES) averaged along the y-axis. b) Reconstructed average y-axis *k* from 9 sky imagers with a distance between imagers of 1.5 km using the Algebraic Reconstruction Technique (ART) method.

4.5 Outline of Testing Layout

For this study, we are interested in reconstructing the 3D extinction coefficient *k (x,y,z)* within a solar forecast domain. Sky imagers can usually provide valuable solar forecast information up to 15 min. Given that cloud speeds from the Large Eddy Simulations (LES) described in Section 4.6 vary between 8 to 10 m/s, domains should be on the order of 5 to 10 km. We chose a cloud domain of 6.4 by 6.4 km horizontal and 5 km vertical size with 50 m horizontal and 40 m vertical resolution for a total of 2,080,768 *k* points.

To better understand the ideal deployments we will also do a sensitivity study. For the sensitivity study we are interested in characterizing the effects of the number of imagers and the distance between imagers. A problem arises when doing such study as the methods to estimate τ_i have errors that are independent of number of imagers and the distance between imagers. For example, it is well documented that clouds are more difficult to detect in the circumsolar region (Yang et al. 2014) and that deployments with fewer clouds in the circumsolar region will perform better. As such, we will remove any random errors associated with the location of the clouds relative to our cameras. To remove this source of error, we used a perfect τ_i defined as

$$\tau_c = Ak_{LES}. \tag{4.12}$$

4.6 Models and Input Parameters

The 3-D reconstruction methods were tested in the virtual testbed from Kurtz et al. (2017). This virtual testbed uses UCLAs LES to model a realistic 3-D atmospheric boundary layer with continental cumulus clouds at high resolution for a time period of 24 hours. Periodic boundary conditions represent infinite domains with the same ground cover, which allows the cloud and atmospheric turbulence to spin up and create realistic cloud shapes and dynamics, such as condensation, evaporation, and deformation. From the LES run, two representative time instances with cloud fractions of 6.8% and 33.3% are selected for reconstruction. The LES liquid water content (LWC) is inputted into the Spherical Harmonic Discrete Ordinate Method (SHDOM) to produce radiance fields (I^{meas}) at a constant SZA of 45°. The SHDOM radiance field reproduces a 1701 by 1701 pixel sky image as obtained through a fisheye lens with an equisolid angle projection as described in section 2.1.

4.7 Sky Imager Deployment Layouts

Aside from assessing the different reconstruction techniques, we are also interested in a sensitivity study to understand the tradeoffs between different SI deployment variables, which are the number of imagers and distance between imagers (Fig. 4.4). A similar study done by Huang et al. (2008) with microwave radiometer (MWR) tomography found that the optimal number of MWR was 4 and that the optimal distance between MWR was 4 km. Nguyen et al. (2014) demonstrated that the optimal distance between imagers for stereography is directly related to the CBH and, as such, the optimal distance between imagers is only valid for the CBH of our test case, which is 0.94 km.

To compare the tradeoffs of using multiple imagers, we simulated 1, 2, 4, and 9 imagers with locations outlined in Fig. 4.4. The 1 imager setup was located at the center of the domain, while the 2, 4 and 9 imager setups are located at distance that minimizes reconstruction error which is 6, 4 and 3 km for 2, 4 and 9 imagers respectively. To obtain the optimal distance between imagers, we tested a setup of 2, 3, 4 and 9 imagers evenly spaced from the center of the domain at distances l= [0.25 0.5 1.0 1.5 2.0 3.0 4.0 6.0] km for the 2, 3, and 4 imager setup, and l= [0.25 0.5 1.0 1.5 2.0 3.0] km for the 9 imager setup.

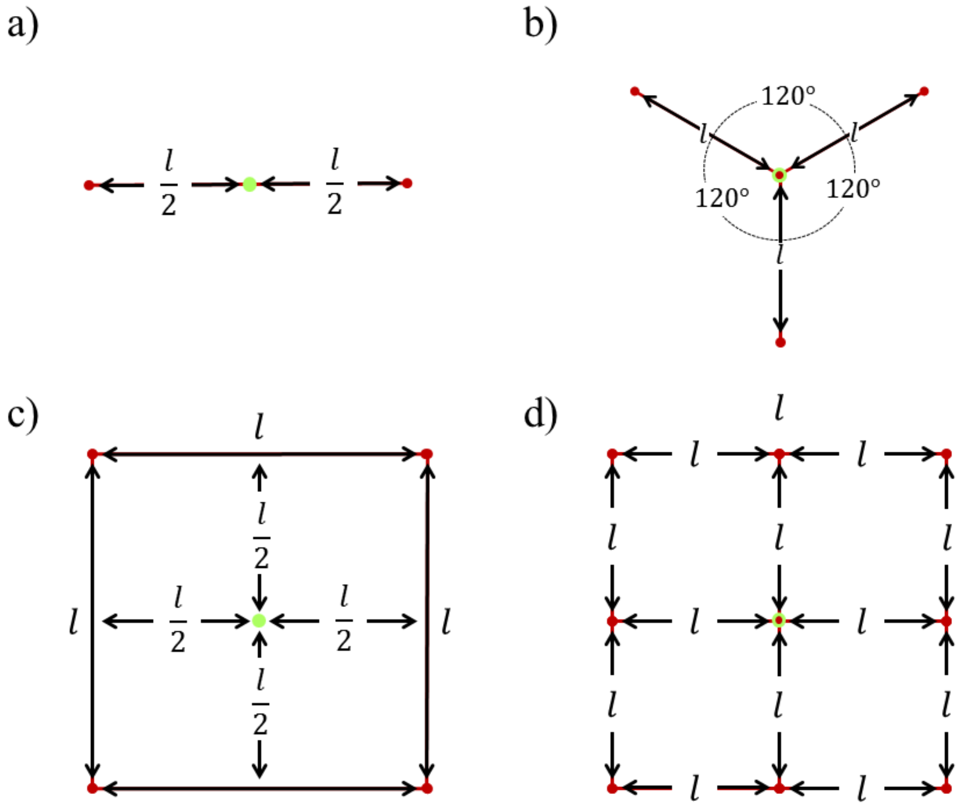

Figure 4.4: Layout of sky imager deployments with different number of imagers and distance (l) between imagers, a) 2 imagers along the x-axis, b) 3 imagers, c) 4 imagers, and d) 9 imagers. Red dots represent imager locations and the green circle (green outline when imager located at center of domain) represents the center of domain.

4.8 Error Metrics

Since measuring cloud properties of real life clouds is extremely challenging one of the main benefits of using simulated test cases is that we are able to validate the errors in spatially-resolved cloud properties. To this end, we are interested in analyzing errors in extinction coefficient, image red (620 nm) pixel brightness, and surface Global Horizontal Irradiance (GHI). The red pixel brightness is used arbitrarily as any of the red, green, blue channels can be used. While perfect k retrievals would automatically result in perfect image pixel brightness and surface GHI, erroneous k retrievals may have different impact on GHI and image errors, which are more relevant in the practice of solar forecasting. We will quantify these errors by calculating the domain MAE and mean bias error (MBE) defined as

$$MAE = \frac{\overline{abs(k_{LES} - k)}}{\overline{abs(k_{LES})}}, \tag{4.13}$$

$$MAE = \frac{\overline{k_{LES} - k}}{\overline{k_{LES}}}, \tag{4.14}$$

where overbars denote averages and *k* can also be replaced with GHI or pixel brightness. For *k*, the averages are over all LES grid points in *x, y, z*. For GHI, the averages are over surface grid points in *x* and *y*. For pixel brightness, the averages are over all pixels of all sky images.

4.9 Validation

Using a 9 imager deployment with a separation of 1.5 km, the ART method is able to decrease the *k* error down to 1.2% and 0.02% after 50 million iterations for a 33% and 6.8% CF respectively. The higher CF case converges slower continuing to decrease in error after 50 million iterations while the low CF case converges after 10 million iterations. These results are dmonstrated in Fig. 4.5. As see in Fig. 4.5 the error of the ART is minimal after 10 million iterations with a correct τ_c input but a correct τ_c is difficult to obtain. The ART method will not correct for any errors and is dependent on the accuracy of the τ_c estimate which for our case is obtained from the RRBR method. To correct for these errors we will use the iterative method described in 4.3.

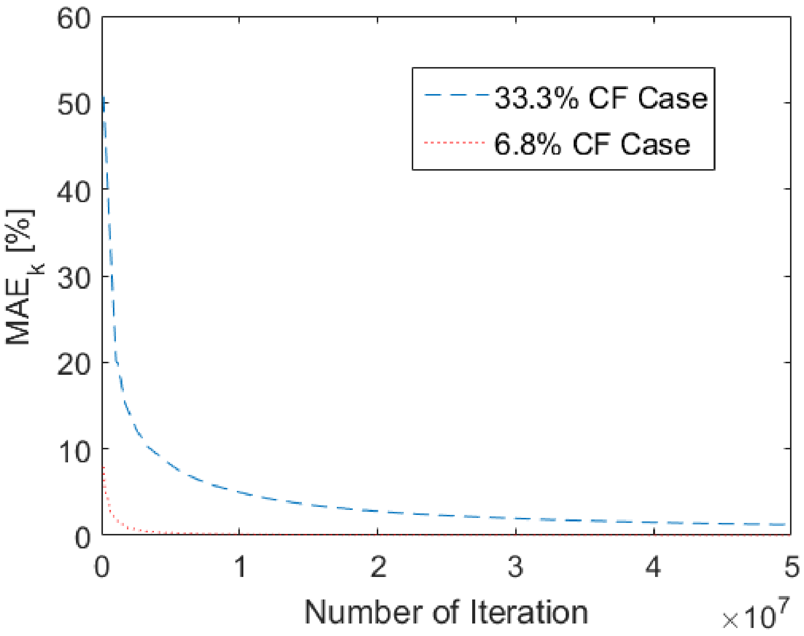

Figure 4.5: Convergence of ART. 33.3% and 6.8% CF test cases represented as the dashed and dotted lines respectively.

To test that the iterative method can converge on a solution we input the correct source function into the method and offset the *k* to see the convergence of the method. Fig. 4.6 demonstrates that the method is able to correctly converge back down to 0.3% and 0.2% image and *k* MAE. The *k* are offset based on using the RRBR method to as an input into the ART method producing a first estimate with error.

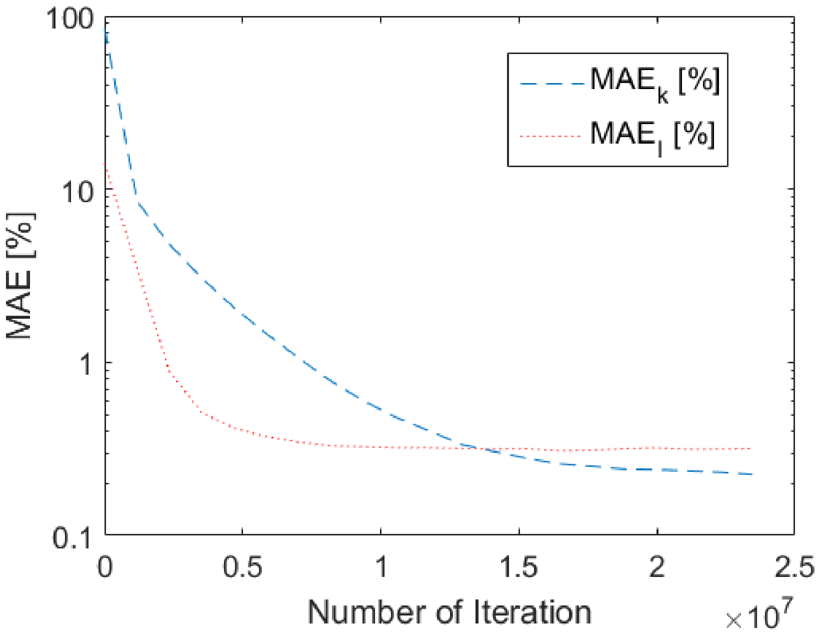

Figure 4.6: Convergence of Iterative method *k* and image errors represented as the dashed and dotted lines respectively.

4.10 Optimal SI Distance Separation

The ART method is used to analyze optimal deployments because of its low computation cost. Using an Intel Core i7-3770 3.4GHz computer the ART methods completes within about 30 seconds as opposed to 2 to 10 days with the iterative method. The ART method (Section 4.2) is applied on a perfect cloud optical depth field as defined in Eq. 4.12. Fig. 4.7 shows that the accuracy of the retrieved *k* increases with the distance between imagers both for *k* and image error. GHI, on the other hand, does not improve after 1.5 km. The error decreases the most between l= 0.25 km and l= 0.5 km; for larger l, the method continues to improve but at a lower rate. Fig. 4.8 and 4.9 demonstrate the results for 4 and 2 imagers, respectively. 4 imagers demonstrated similar results to Huang et al. with an optimum between 2 km$< l <$4 km for *k*, GHI and image error perform worse as l increases beyond 4 km. The 2 imager setup continues to improve with increased separation. This suggests that for solar forecasting a 1 km seperation is sufficient for accurate GHI estimation while for accurate *k* larger separation is needed.

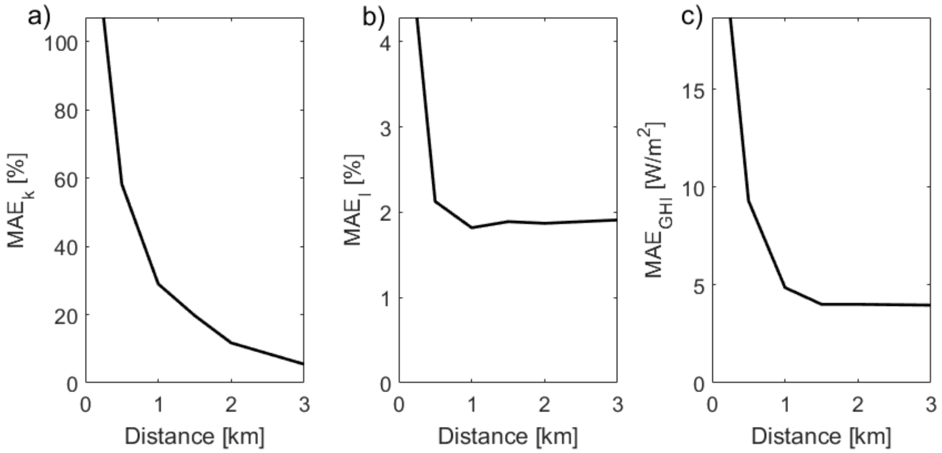

Figure 4.7: Domain averaged mean absolute error in (a) k, (b) image pixel error, and (c) Global Horizontal Irradiance (GHI) for retrievals with 9 imagers at different distances l.

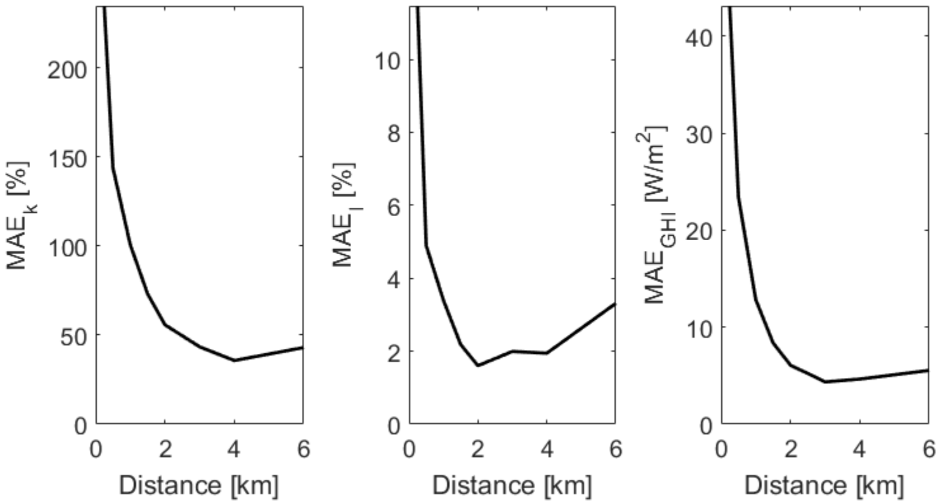

Figure 4.8: Domain averaged error in extinction coefficient k (a), image pixel error (b), and Global Horizontal Irradiance (GHI) (c) for retrievals with 4 imagers at different distances l.

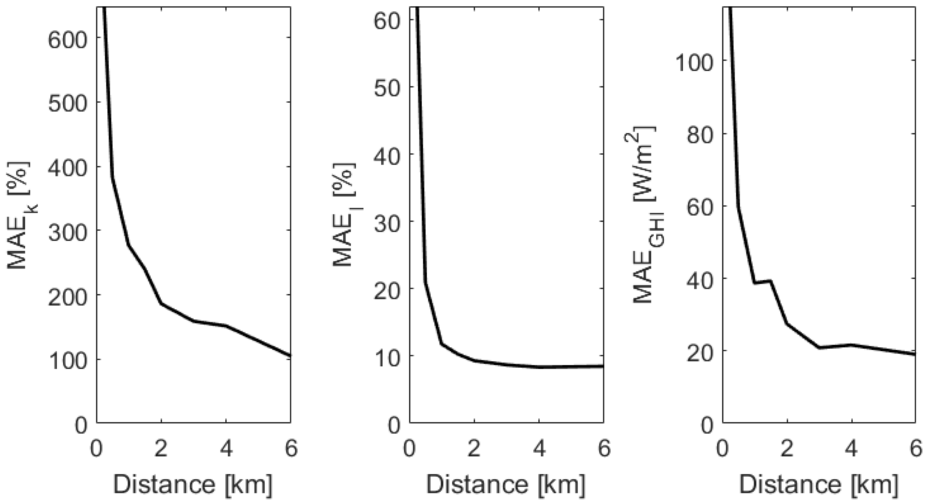

Figure 4.9: Domain averaged error in extinction coefficient *k* (a), image pixel error (b), and Global Horizontal Irradiance (GHI) (c) for retrievals with 2 imagers at different distances l.

4.11 Optimal number of SIs

As seen in Fig. 4.10, the number of SIs improves the overall reconstruction of the cloud domain. Similar to Huang et al., we observe a large performance increase when using 4 imagers compared to 2 or 3, and less improvement with additional imagers.

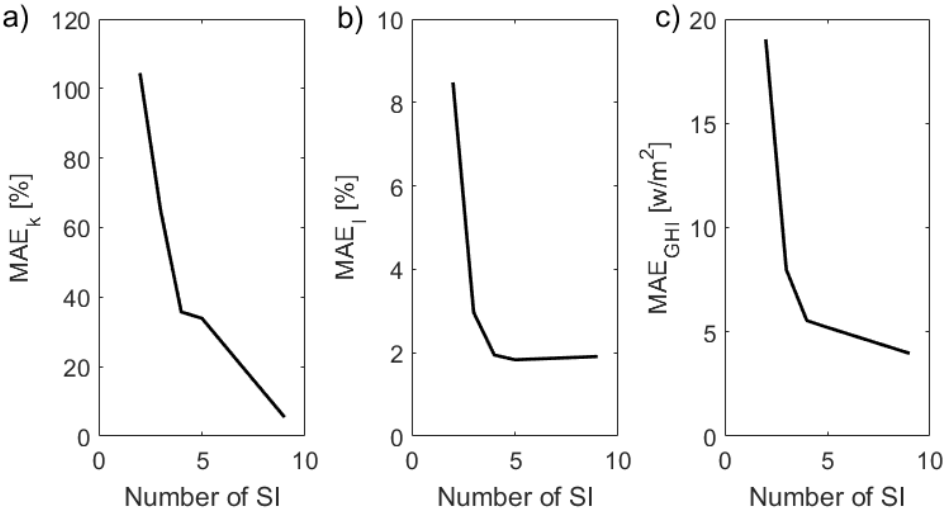

Figure 4.10: Domain averaged error in extinction coefficient *k* (a), image pixel error (b), and Global Horizontal Irradiance (GHI) (c) for retrievals with 2, 3, 4, 5 and 9 imagers at their respective optimal separation.

Although improvements in GHI and image pixel error between 4 and 9 imagers are minimal for an ideal case, using 9 imagers greatly increases the robustness of the cloud scene reconstruction in real applications. Two mechanisms are expected to benefit tomographic methods applied to 4 or more imagers in real applications. The first is that dirt on the dome of one imager does not contaminate the results. In single-imager cloud decision, dirt is often identified as a cloud since its red-blue-ratio is closer to clouds than clear sky. The ART limits the impact of the dirt because the only solution that can satisfy a spot in one image that is not present in any other images is a cloud located immediately above the imager. Such a low cloud would be invisible to the other imagers as data at large zenith angles is poorly resolved and therefore excluded. The constraint on minimum

CBH then results in the clearing of that cloud (see Sec 4.4). The second is that using data from the circumsolar region becomes unnecessary. As stated previously (section 4.1) the circumsolar region in the sky hemisphere is a common source of error. With 9 imagers, it is possible to ignore the circumsolar region in every imager as the neighboring imagers are able to fill in the missing data for the circumsolar region. Fig. 4.10 demonstrates that in an ideal case there are minimal improvements in 3-D reconstruction when more than 4 imagers are available, but removing the pixels with less than a 30°solar pixel angle i.e. scattering angle (SPA) in each image, the error increase by over 50% for 5 or less imagers but almost equals the solution for images including the solar region for 9 imagers. This suggests that for real deployments, at least 9 imagers are recommended.

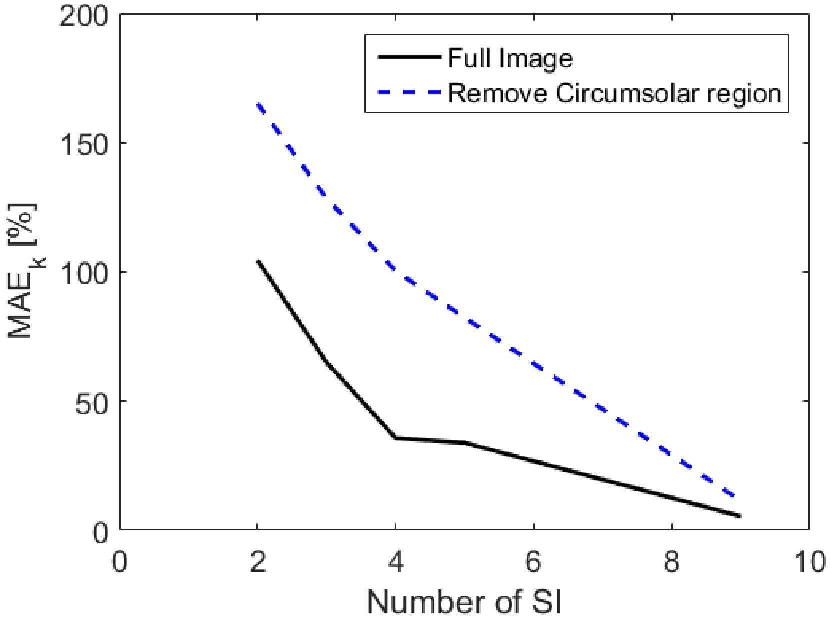

Figure 4.11: Domain averaged error in *k* for retrievals with 2, 3, 4 and 9 imagers using the full image (same as Fig 4.10. (a) in black) and removing the circumsolar region with SPA$<$ 30° in each image.

Fig. 4.12 demonstrates the various ground based irradiance calculated from the reconstruction at various distance separation and number of imagers. Fig. 4.13 demonstrates the various reconstructed cloud scenes as a vertical average at various distance separation and number of imagers. Fig. 4.14 demonstrates the various reconstructed cloud scenes as a average in the x direction at various distance separation and number of imagers.

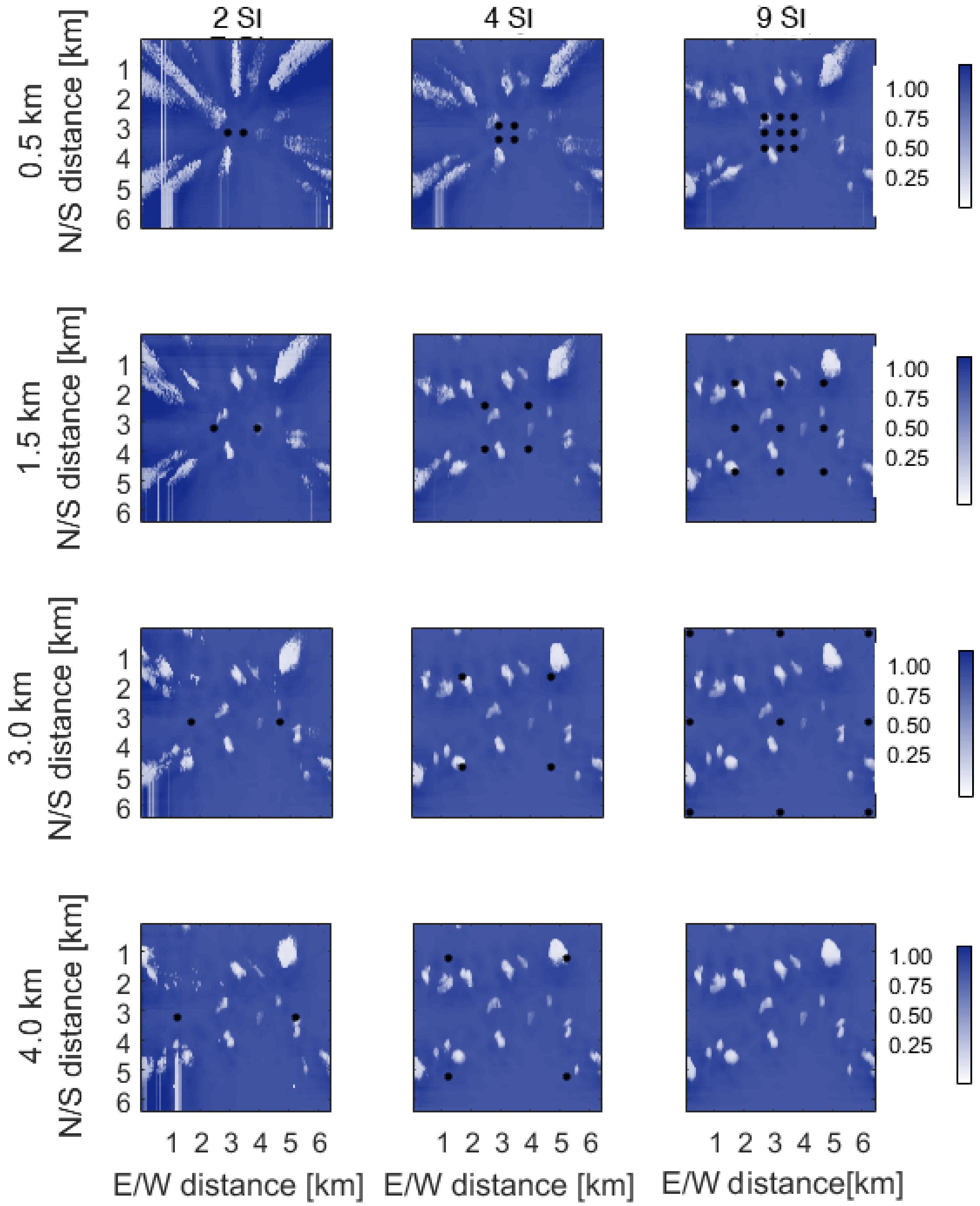

Figure 4.12: Spherical Harmonic Discrete Ordinate Method (SHDOM) simulated clear sky index (kt) from the reconstructed extinction coefficient field from different number of imagers (columns) at different l (rows). Black dots represent imager locations.

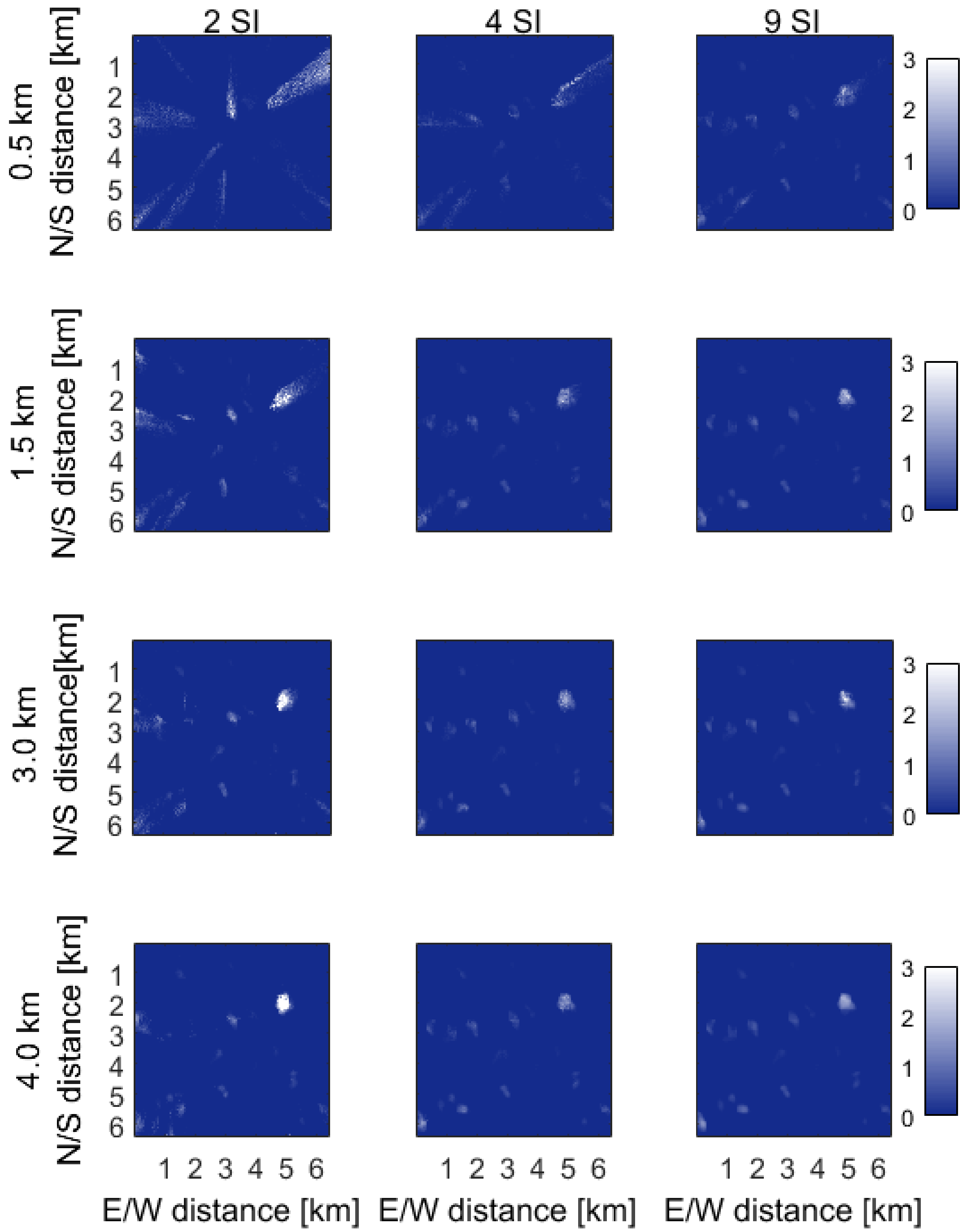

Figure 4.13: Reconstructed vertically averaged extinction coefficient *k* from different number of imagers (columns) at different l (rows). The bottom right graph is the correct *k*.

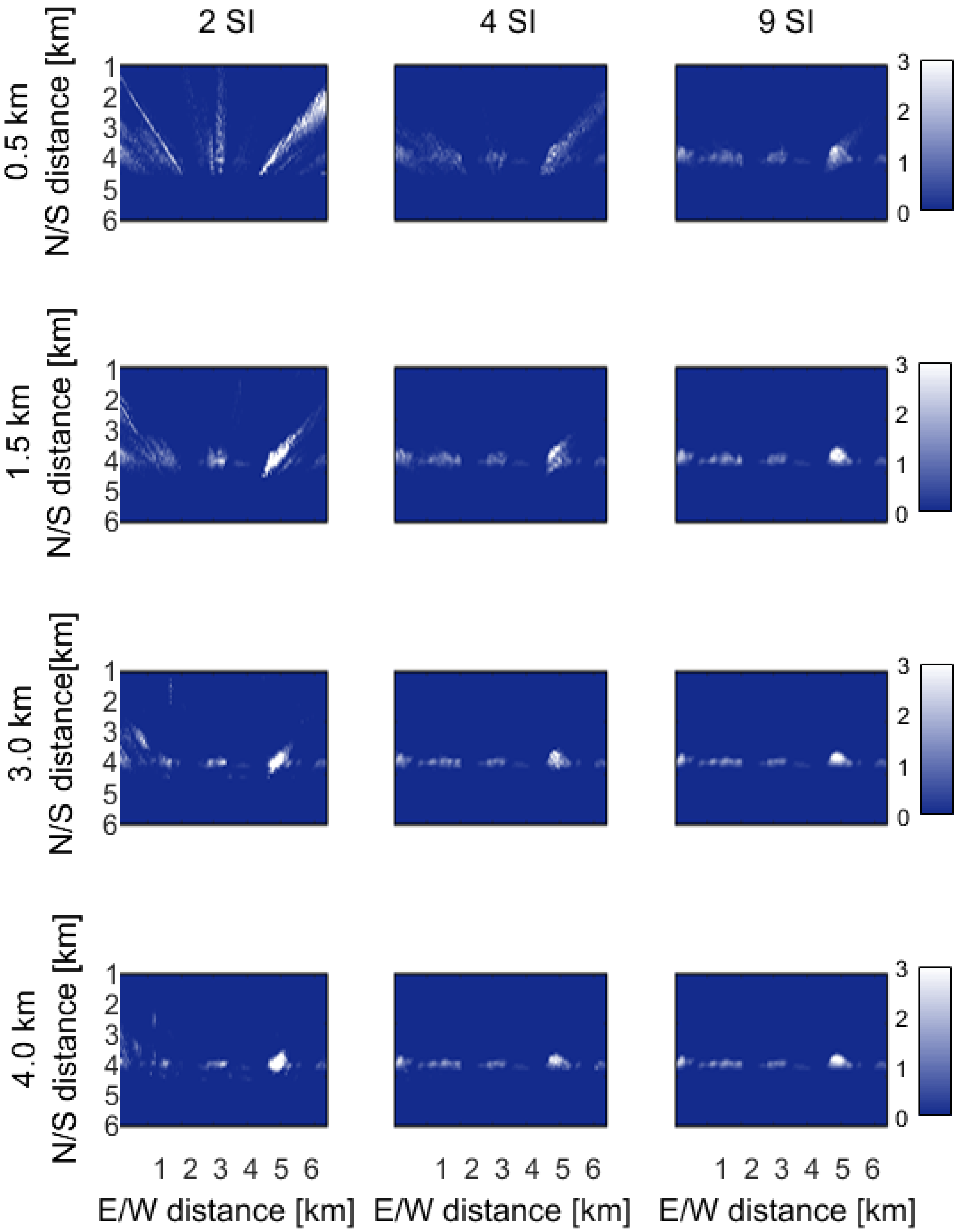

Figure 4.14: Reconstructed extinction *k* averaged in the x direction from different number of imagers at different l, bottom right is correct *k*.

4.12 3D Reconstruction Methods

To isolate characteristics of the reconstruction methods, we now focus on a specific deployment. We will focus our attention on a 9 imager deployment with l = 1.5 km. We use 9 imagers because this is the optimum scenario to demonstrate the limitations of the methods and not the deployments, while maintaining l = 1.5 km since it becomes increasingly difficult to obtain permissions to install camera systems away from the location of interest. For example, at a utility scale power plant with a typical dimension of 2 × 2 km, l = 3 km would require obtaining permissions from adjacent property owners.

4.13 Results of Algebraic Reconstruction Technique

As described in section 4.2 the ART method requires an input τ_c to calculate k. For this section we will use the RRBR (Mejia et al. (2016)) method to obtain an estimate of τ_c. The RRBR method uses both radiance and red blue ratio values to estimate τ_c based on a homogenous cloud look-up table of SHDOM simulations. Since the RRBR is based on a homogeneous clouds it has a propensity to underestimate τ_c because on average homogeneous clouds are darker than heterogeneous clouds. This underestimation in τ_c is seen in Fig. 4.15 and Table 4.1 as the k MBE is -17.1%. MAE for k is 53.4% while the GHI MAE is significantly lower at 1.53%.

Table 4.1: Error statistics of Algebraic Reconstruction Technique (ART) and iterative method. MAE[%] is the relative mean average error, and MBE [%] is the relative mean bias error. DNI is the Direct Normal Irradiance and GHI is the Global Horizontal Irradiance. k is the extinction coefficient and τ is the vertical sum of k.

	ART	Iterative method
τ MAE[%]	34.8	17.2
τ MAE[-]	0.0481	0.0238
τ MBE[%]	-17.1	-2.8
k MAE[%]	53.4	33.6
k MAE[-]	0.00025	0.00015
k MBE[%]	-17.1	-2.8
GHI MAE[%]	1.53	0.85
GHI MAE[-]	10.1	5.6
GHI MBE[%]	-0.04	0.12
GHI($k_t < 0.98$) MAE[%]	21.8	0.86
GHI($k_t < 0.98$) MAE[-]	68.9	2.7
GHI($k_t < 0.98$) MBE[%]	14.2	0.15
DNI MAE[%]	1.3	0.81
DNI MAE[-]	10.5	6.5
DNI MBE[%]	0.46	0.32
Image Pixel MAE[%]	4.3	1.1
Image Pixel MBE[%]	-1.3	-0.6

Removing all grid points with $k_t > 0.98$, the MAE of GHI increases to 21.8%. Most cloudy grid points are correctly identified with 98.8% of k being correctly separated as k=0 or $k \neq 0$ (Table 2). k voxels that are misidentified are either thin clouds (τ <0.5), e.g. in the north west of the domain (as seen in Fig. 4.17) or at the edges of clouds.

Table 4.2: Contingency table of observed extinction coefficient and reconstructed Algebraic Reconstruction Technique (ART) extinction coefficient, k.

ART/ Observation	$k = 0$	$k \neq 0$
k = 0	94%	0.8%
k$\neq$ 0	0.4%	4.8%

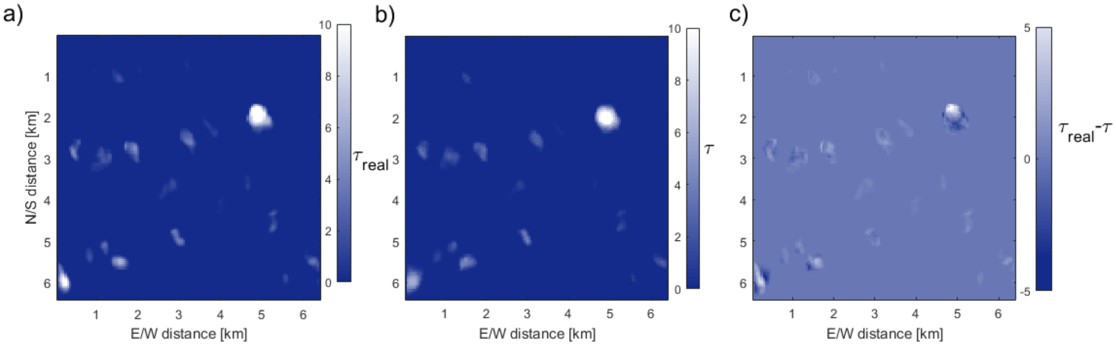

Figure 4.15: Vertical sum of k (τ), from Large Eddy Simulations (LES) (ground truth), a), reconstructed from Algebraic Reconstruction Technique (ART), b), and their difference (c). North (N) is up and East (E) is to the right per convention.

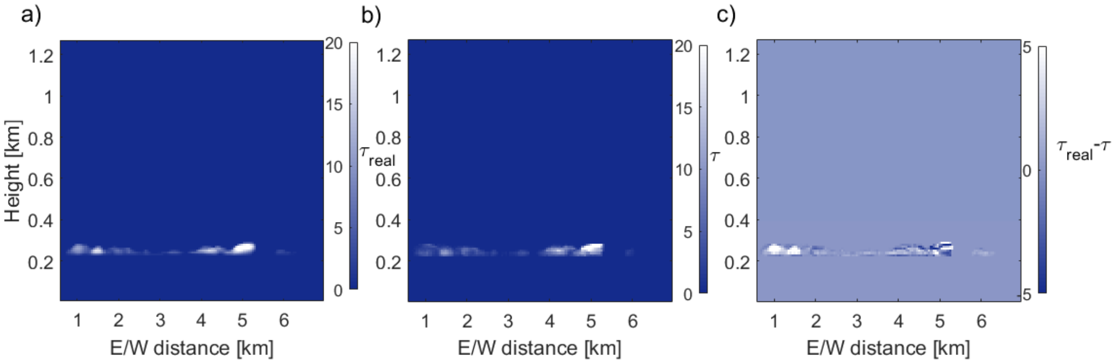

Figure 4.16: N/S sum of k from LES (ground truth, a), reconstructed from ART (b), and their difference (c). North (N) is up and East (E) is to the right per convention.

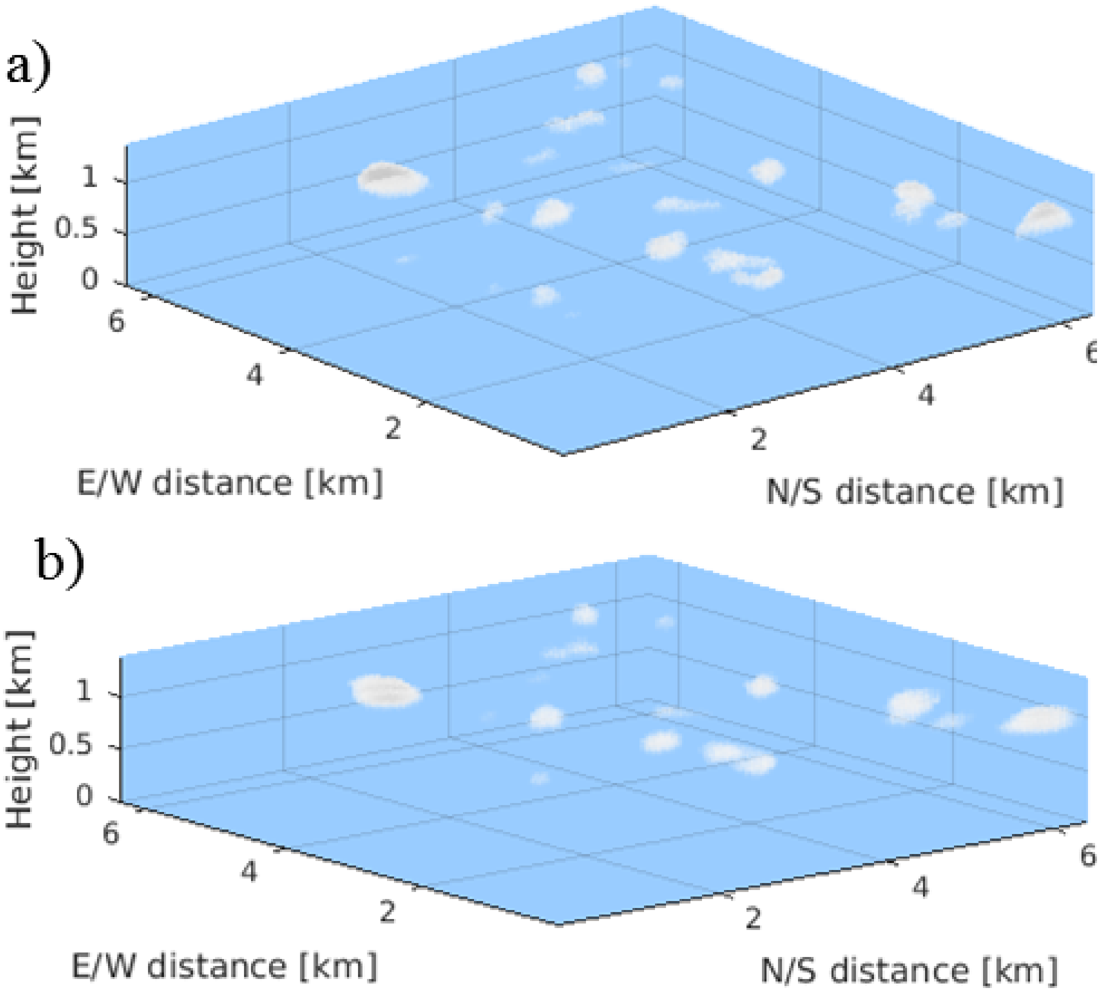

Figure 4.17: 3-D depiction of reconstructed k from the Algebraic Reconstruction Technique (ART) (a) and ground truth (b).

4.14 Results of Iterative retrieval

The iterative method is based on the assumption that iteratively minimizing the image error further minimizes the extinction coefficient errors. To decrease the computational cost, *k* from the ART method is input to the iterative method providing an accurate first estimate. Fig. 4.18a) demonstrates that the iterative method further decreases the image error. After 13 iterations, the image MAE decreases from 4.3 to

0.7% and 13.2% to 7.0% for the 6.8% and 33.3% CF cases respectively. The *k* MAE also decreases with the decrease in image error going from 53.4% to 33.6% and 83.2% to 66.4% in the 6.8% and 33.3% CF cases respectively.

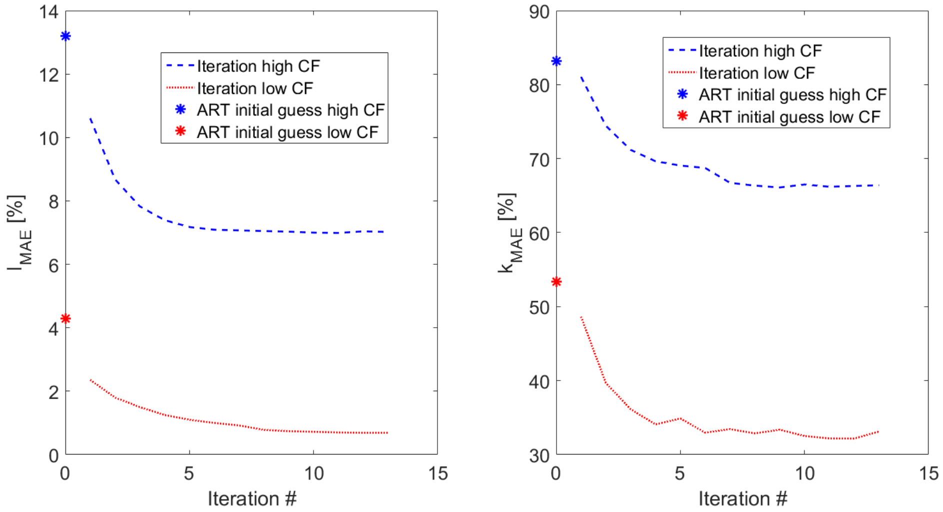

Figure 4.18: (a) Image pixel red brightness mean average error (MAE) for each iteration. (b) MAE of *k* at each iteration.

The iterative method decreases the error from the initial ART estimate. *k* MAE decreases nearly 20 percentage points and 36%. The under-predictive tendencies are resolved with the *k* MBE improving from -17.1% to -2.8%, the MAE GHI of cloudy regions improving from 21.8% to 0.85%, and the MBE GHI of cloudy regions improving from 14.2% to 0.15%.

4.15 Application to solar forecasting

Table 4.1 demonstrates that the MAE in GHI is small compared to the error in *k* for both the ART and the iterative method. For atmospheric science applications, this means that the methods require further improvements to provide high quality 3-D cloud reconstructions. For solar energy applications, surface GHI is the more important value, and as such the ART method is well suited for solar forecasting.

To demonstrate the potential of the ART for solar forecasting applications, the GHI map from the ART method in section 4.13 is advected using the average cloud speed from the LES. Fig. 4.19 demonstrates MAE of persistence, conventional SI and the ART forecasts relative to the ground truth measurements from the LES. In less than 1 minute forecast horizon, the ART method beats persistence in terms of MAE. The magenta line demonstrates a forecast using a conventional 2-D cloud representation and trinary cloud decision (Yang et al. 2014). The ART method significantly improves upon the conventional method at nowcast (0 minute forecast) and throughout the first 2 minutes of forecast. The improvements are due to better representation of 3-D clouds as well as the use of a *k* instead of a trinary system. At longer forecast times, the clouds evolve in shape and thickness and the advantage of better cloud initial conditions decreases.

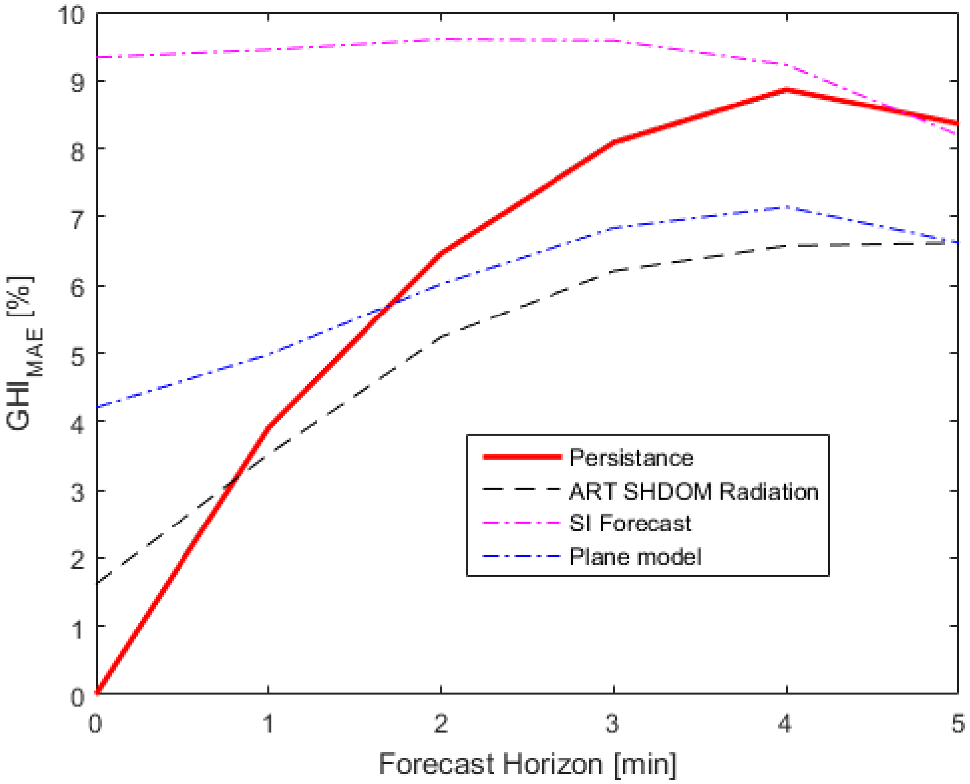

Figure 4.19: Global Horizontal Irradiance (GHI) forecast mean average error (MAE) for persistence forecast in red, state-of-the-art forecast in magenta, and Algebraic Reconstruction Technique (ART) forecast in black. The persistence forecast assumes that the current GHI persists for the next 5 minutes. For ART GHI forecasts, the 3D reconstructed k field is first advected with the Large Eddy Simulation (LES) cloud speed. Then Spherical Harmonic Discrete Method (SHDOM) 3-D radiative transfer simulations yield surface GHI.

Acknowledgements

Chapter 4 is currently in being prepared for submission for publication of the material. F. A. Mejia, B. Kurtz, and J. Kleissl, Cloud tomography applied to sky images: Part I: A virtual testbed. The dissertation author was the primary researcher and author of this material.

Chapter 5

Cloud tomography applied to sky images: Part II: A real world case study

5.1 Outline of testing layout

As demonstrated in an ideal case in Mejia 2017 et al. a 3D cloud reconstruction can be made using multiple camera images in an ideal case. The findings demonstrated that having more imagers improves a 3D reconstruction but after 4 sky imagers improvements significantly decrease. Similar to this, it was found that an increased separation between imagers resulted in improved reconstruction accuracy. At a distance separation of 1.5 km most of the improvements may be obtained. Based on these results and available locations, 5 UCSD sky imagers (USI) were deployed across UCSD and nearby areas as demonstrated in Fig. 5.1. Considering USI 1.1 the center of the domain the four other imagers had an average distance of 1.315 km from the center of the domain. To analyze these methods on real imagers we will use the 4 outer imagers (excluding the center imager) for cloud reconstruction and use the center imager for error analysis and validation.

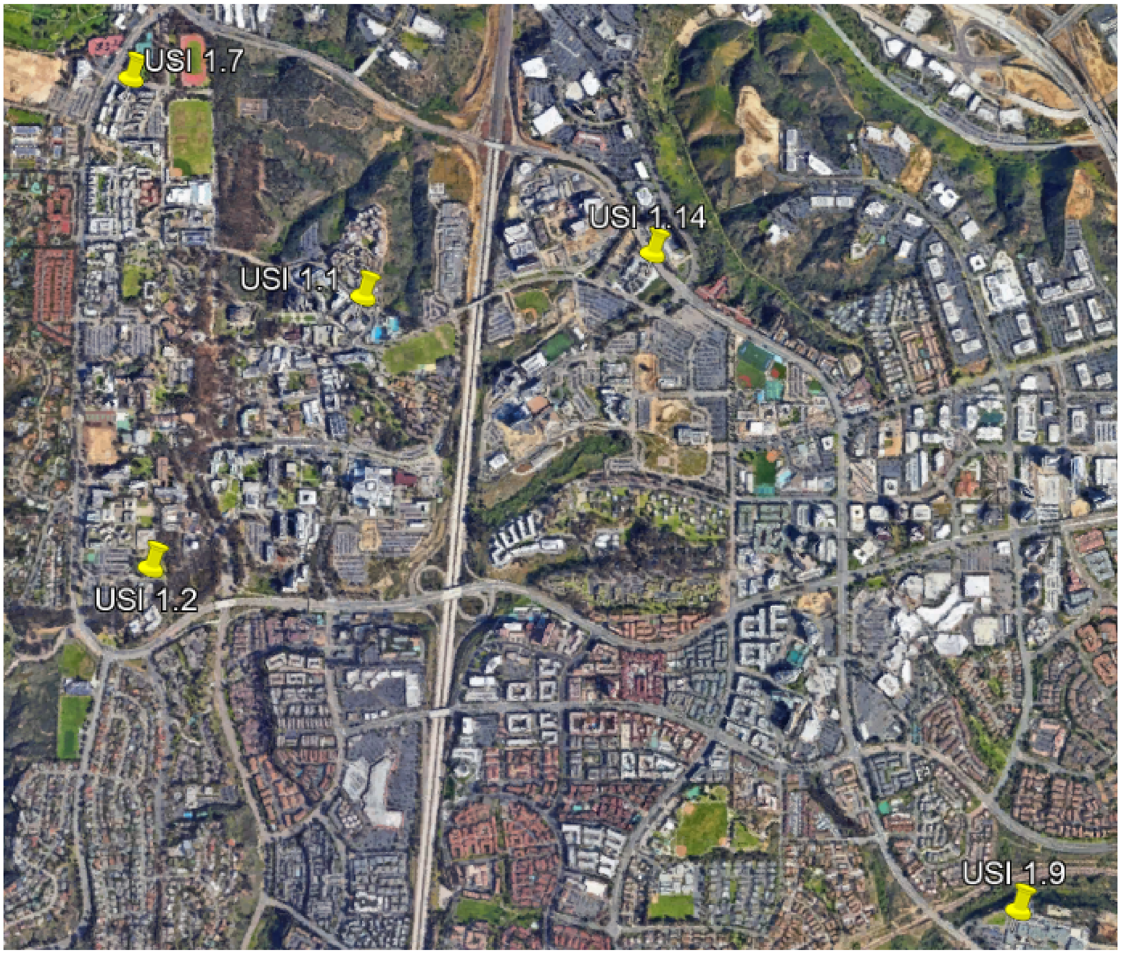

Figure 5.1: Map of real world deployed UCSD sky imagers

5.2 Topographic obstruction

In real world imagery, it is commonly observed that topographical variations result in image obstruction. Buildings, trees and hills may block the sky from the imager decreasing the information obtained by the reconstruction. To analyze this, we reconstructed a simulated cloud scene with the locations of the deployments described in section 5.1 but removing pixels with a pixel zenith angle (PZA) greater than a threshold.

By removing PZA greater than a value between 40-85 we are estimating the results of obstructions in the horizon. We are mainly focusing on obstructions in the horizon, as those are normally caused by factors that cannot be changed by relocating the imager, as opposed to simply moving an imager to a roof to be above a small tree. Fig. 5.2 demonstrates the increase in error as more of the image is obstructed. Up to a PZA of 75 the reconstruction is unchanged and removing these parts of the image results in no change. From here there is a notable increase in error from a PZA of 50-75. If an obstruction of more than 50° PZA is observed the reconstruction is no longer accurate as the errors in *k* are greater than 100%.

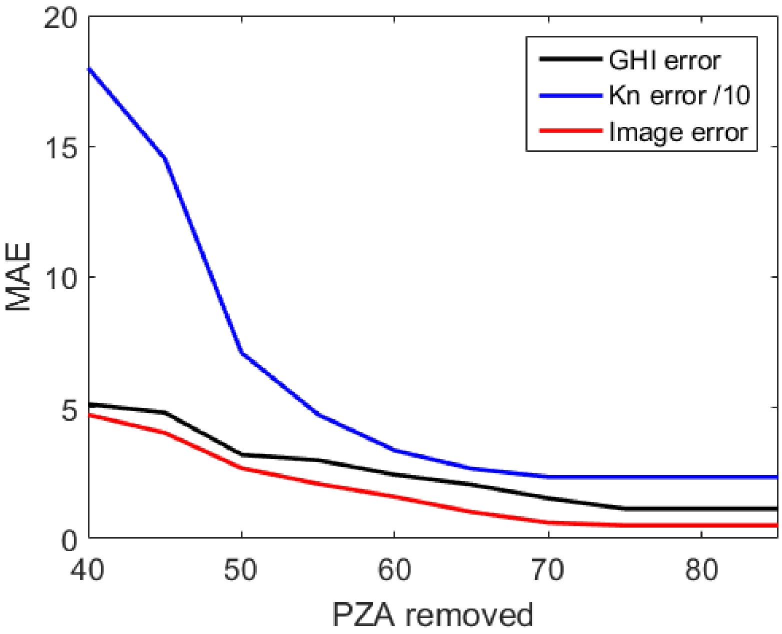

Figure 5.2: Domain averaged error GHI, *k* and image error as a function of obstructed PZA. 40 represents a reconstruction were pixels with PZA greater than 40 were not used for the reconstruction.

5.3 Solar region

It has been observed that the area of a sky image close to the sun (circumsolar region) is difficult to distinguish between various forms of clouds and clear sky. This is both a characteristic of the circumsolar region (Mejia et al.) as well as a result of stray light, light that is scattered from dust or within the optics that causes errors in the radiance measurement. Since this region causes a large uncertainty, we are interested in knowing how much of this region we can remove before significantly loosing information for the reconstruction. To do this we analyzed the same simulations as in section 5.2 but this time we removed pixels with solar pixel angles (SPA) less than a threshold. Fig. 5.3 demonstrates the increase in error as we remove more of the image. There is no increase in error when removing less than 10° SPA. The error begins to increase after 10° SPA and takes a significant jump after a SPA of 30°. This suggests that we can ignore pixels with SPA less than 10° without losing accuracy in the reconstruction; as such we will remove these pixels from the images that we use.

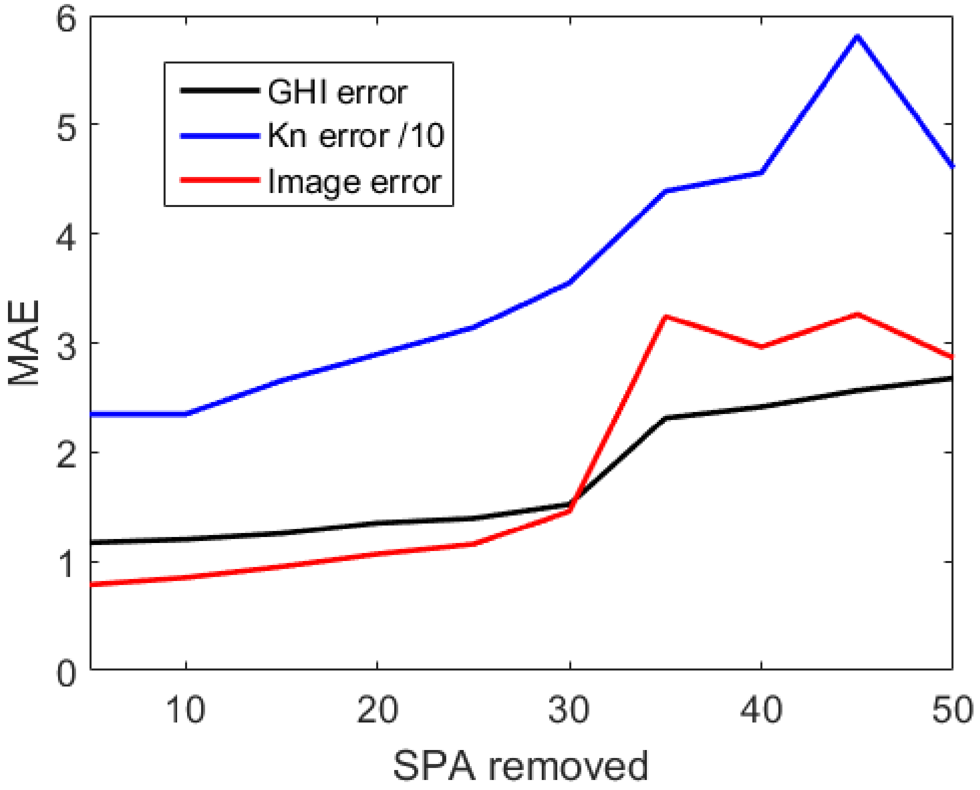

Figure 5.3: Domain averaged error GHI, *k* and image error as a function of circumsolar region removed. 20 represents a reconstruction were pixels with SPA smaller than 20 were not used for the reconstruction.

5.4 ART

Fig. 5.4 demonstrates the real image and the simulated image from a reconstructed cloud field. It is important to note that Fig. 6 (a) was not used for the reconstruction and is only used for validation. To vertically constrain the cloud domain, measurements from a ceilometer located in the center of the domain were used, with an output of 950m. Using a 10% uncerntainty we constrain the cloud base height to 90% of the Ceilometer measurement or 820m (rounding to the lowest voxel). Using local soundings at 12:00:00 UTC we constrain the cloud top height based on the atmospheric inversion which is

1060m (rounding to heighest voxel). The reconstructed cloud has a MAE for the image in the red wavelength (620 nm) of 28.9%. It is able to get the general shape of clouds but struggles with small clouds and holes inside of clouds. Small clouds are difficult for the method since errors in geometric calibrations lead to the clouds being identified in different locations, resulting in small clouds not being identified. Another large source of error is the circumsolar region. Because of its high-peaked source function it is dificult to simulate the solar region. As well as this there is stray light that causes the circumsolar region to be brighter than simulations. To remove this source of error we will exclude the circumsolar region from the error analysis, removing pixels within a solar pixel angle of 150. This decreases the error down to 22.9%.

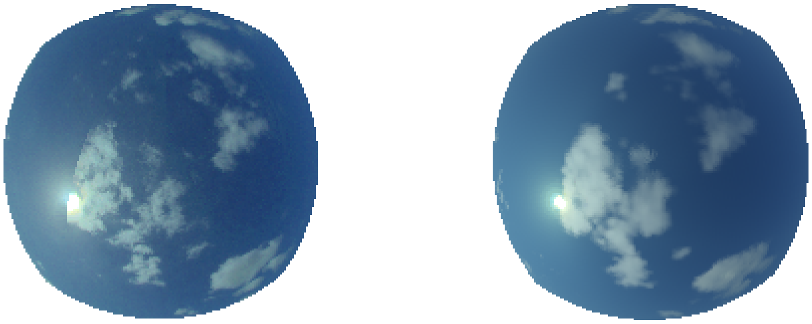

Figure 5.4: (a) Real USI image taken at center of domain corresponding to USI 1.1 in Fig. 1 on April 14th 2017 at 17:03:00 UTC. (b) Simulated image from reconstructed cloud field using imagers 1.2, 1.9 1.14 and not USI 1.1.

Fig. 5.5 demonstrates an image that was used for the reconstruction. Since this image was used for the reconstruction the accuracy of the simulated image increases and the MAE goes down to 20.8%.

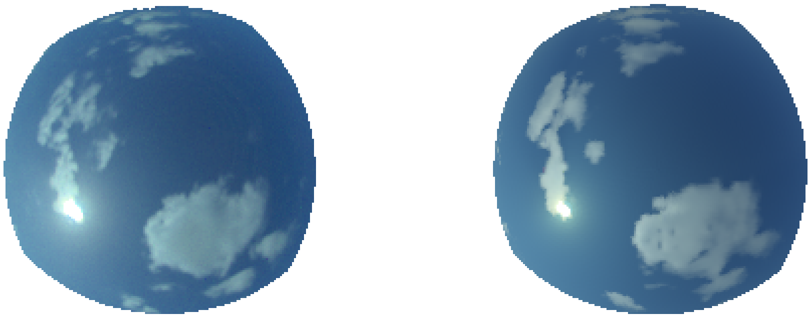

Figure 5.5: (a) Real USI image taken at center of domain corresponding to USI 1.2 in Fig. 1 on April 14th 2017 at 17:03:00 UTC. (b) Simulated image from reconstructed cloud field using imagers 1.2, 1.9 1.14 and not USI 1.1.

Fig. 5.6 demonstrates a timeseries of the reconstructed 3-D cloud scene as well as the ground truth and simulated image.

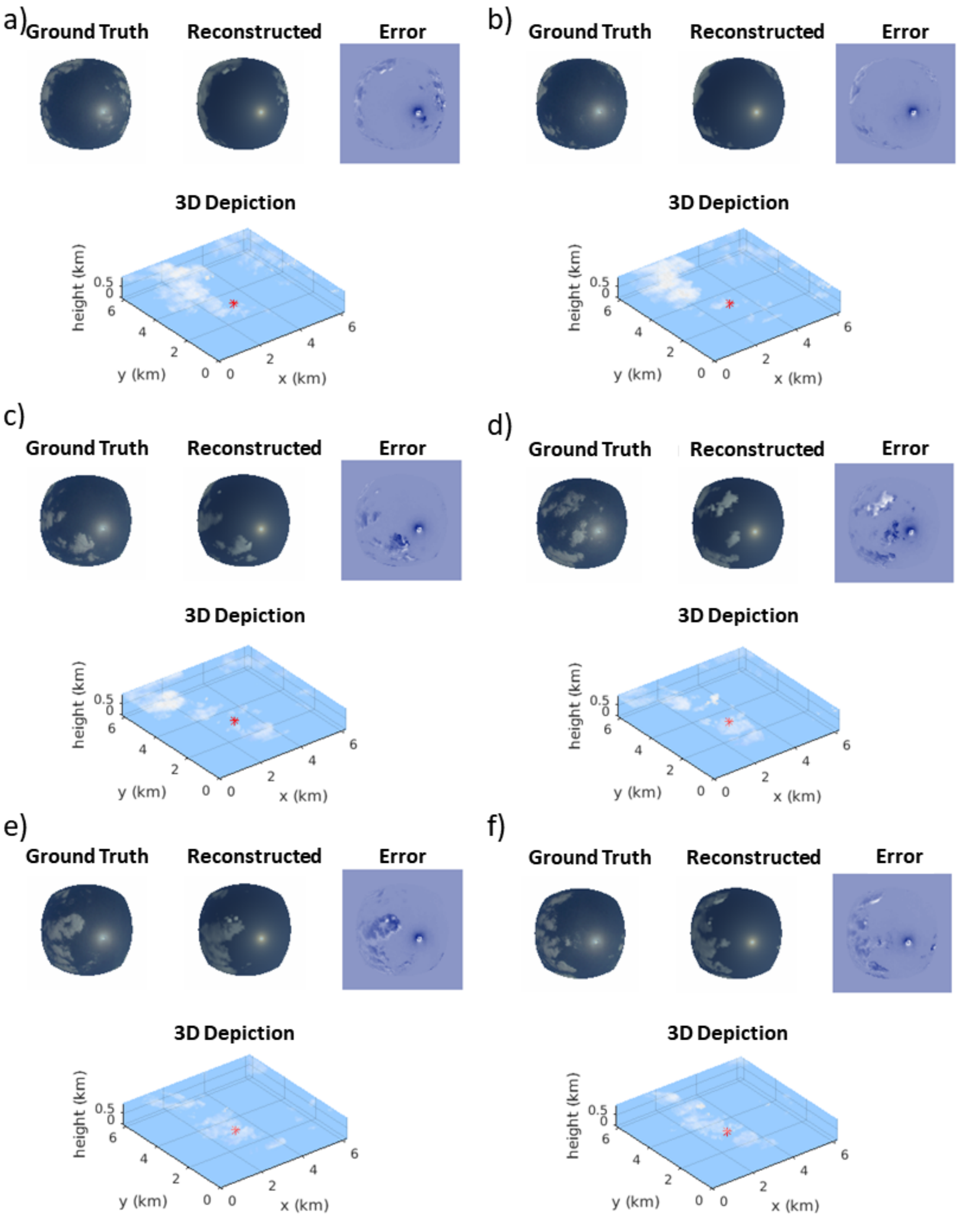

Figure 5.6: Timeseries of ground truth images, reconstructed images, image error and 3-D cloud depiction for (a) May 14th 2017 at 18:00:00 UTC (b) May 14th 2017 at 18:02:30 UTC (c) May 14th 2017 at 18:05:00 UTC (d) May 14th 2017 at 18:07:30 UTC. (e) May 14th 2017 at 18:10:00 UTC (f) May 14th 2017 at 18:12:30 UTC.

Acknowledgements

Chapter 5 is currently in being prepared for submission for publication of the material. F. A. Mejia, B. Kurtz, and J. Kleissl, Cloud tomography applied to sky images: Part II: A real world case study. The dissertation author was the primary researcher and author of this material.

Chapter 6

Conclusion

Using 3D radiative transfer models we have been able to explore the geometric and cloud parameters that affect whole sky imagery. Synthetic images demonstrate that SZA, τ_c, SPA, and SZA all significantly and often non-linearly and non-monotonically affect radiance I_λ and RBR of sky image pixels. For thin clouds, $I_\lambda(SPA)$ increases rapidly as it approaches the sun, as a result of the strong forward peak in the cloud phase function. On the other hand, for thick clouds $I_\lambda(SPA)$ is found to be near constant with solar pixel angle for $\tau_c > 30$. PZA has two main effects, horizon brightening for thin clouds, and horizon darkening for thick clouds. Thick clouds fall in the diffusion regime where I_λ decreases with PZA, but is independent of other parameters.

At a SZA of 45° is demonstrated to increase with increasing τ_c for thin clouds. It reaches a peak at a τ_c between 0-5, depending on SPA and PZA. At τ_c greater than 5, $I_\lambda(\tau_c)$ decreases with increasing τ_c. Similar characteristics are observed for the RBR although it does not decrease as much after reaching its maximum, making it an effective tool for distinguishing between clear sky and thick clouds. However, neither $I_\lambda(\tau_c)$ nor $RBR(\tau_c)$ are monotonic, leading to the difficulties in cloud detection and τ_c characterization with one parameter. The RRBR method combines the RBR and I_λ to overcome the non-monotonic nature of each individual parameter.

Summary statistics of the different comparisons are presented in Table 3.1. For overcast skies the RRBR yields τ_c that are consistent with the Min et al. method. For heterogeneous cloud fields (cloud fraction < 0.7), comparisons with microwave radiometer (MWR) measurements of LWC at zenith demonstrated that the RRBR method provides τ_c estimates with typical R2 of 0.68 and RMSE of 2.2 which is well within the uncertainty of the MWR instrument (± 5.6) but more work needs to be done to validate that heterogeneous clouds are within the 21% uncertainty required for solar applications. As demonstrated by the relative RMSE in Table 3.1, the RRBR method provides accurate τ_c for overcast thick clouds. The relative RMSE is larger for $\tau_c < 10$ for all comparison datasets and future development requires a new comparison method for thin clouds. These results validate the RRBR method for overcast clouds but consistent under-predictions of heterogeneous cloud optical depth requires improvement in the method.

Characterizing the cloud heterogeneity effects may improve the RRBR method. As the RRBR method is based on interpolants developed from simulations of homogeneous overcast skies, cloud heterogeneity violates the assumptions and is likely the leading source of errors. Errors due to cloud heterogeneity have been analyzed mainly in the context of satellite remote sensing. Varnai et al. (1998) and Chambers et al. (1997) observed that the cloud spatial reflectance variation is smoother than variations in τ_c. They hypothesized that optically thicker clouds would scatter more light to their thinner neighboring clouds causing the thinner clouds to appear brighter and thicker (looking from space), while the thinner clouds would scatter less light to the thicker clouds making them appear darker and thinner than expected for a homogeneous cloud scene. A similar but opposite effect is observed in ground based imagery, where thicker clouds shade their neighboring thinner clouds making them appear darker and thicker but this effect is moderated by the location of the sun relative to the clouds. Fig. 3.5 also shows that sun-facing cloud edges scatter more light, increasing I_λ, and leading to thinner τ_c estimates than the cloud edges on the opposite side. Cloud edges facing away from the sun will be shaded by the rest of the cloud and will be estimated as being thicker. These 3-dimensional effects introduce noise in RRBR estimations of τ_c. Although the comparison methods presented here are able to highlight some errors in the RRBR method no method was accurate enough to provide information about thin clouds ($\tau_c < 10$) and future development requires a new comparison method for thin clouds.

With the ability to obtain pixel-by-pixel τ_c estimates we are able to expand on this to estimate the 3-D distribution of clouds in the atmosphere through tomographic methods. Summary statistics of the ART and the iterative methods are presented in Table 1. The k MAE is 53.4% using the ART and decreases to 33.6% after 41 iterations of the iterative method. The ART method using τ from the RRBR method reflects the under-predicting tendencies of the RRBR as demonstrated by the -17.1 MBE of k. Although the iterative method decreases the error, the computational cost is high as it takes 37 days to reconstruct 1 cloud scene, while the ART method takes 30 seconds. The range in days is directly related to the cloud fraction as more cloud voxels must be solved. For this reason the ART is used for solar forecasting applications. The ART method is demonstrated to beat persistence at a 1 minute forecast horizon, demonstrating its potential for solar energy applications.

We have introduced tomographic methods to multiple sky images to reconstruct 3-D fields of extinction coefficients by using simulations of images in an atmosphere created from 3-D heterogeneous cloud scene from LES. As expected, more imagers increases the accuracy of a 3-D cloud reconstruction. This is especially true for up to 4 imagers after which the benefits of more imagers decrease. Although having more imagers improves the accuracy of the 3-D reconstruction, it also increases the capital and operations and maintenance cost of the imagers, creating a tradeoff between having more imagers and improving accuracy. The distance between imagers also plays an important role in reconstruction accuracy. In these idealized scenarios with a 1 km cloud height, an increase in separation between imagers led to an increase in 3-D reconstruction accuracy up to 3 km. This is because a diversity in perspectives better constrains cloud dimensions. It is important to note that these conclusions are for an idealized image and these results need to be validated in real images as well as to account for both topographic obstructions and non-ideal lens distortion. As buildings and trees commonly obstruct the horizon in an image imagers where the cloud appears at a large zenith angle may not contribute to the reconstruction of that cloud. Further, cases with clouds or obstructed by other clouds as in multiple cloud layers need to be investigated.

Using UCSD solar testbed 5 sky imagers were deployed across UCSD and nearby areas. Images from 4 of the cameras were used to reconstruct 3D clouds and compare to the fifth camera. A comparison between the simulated reconstructed image and ground truth image led to a 22.9% error. Sources of real world errors were also explored. Topographic obstruction were found be within 2% of ideal error with at least a field of view of 70 °. This was done by removing parts of the image representative of trees and building in an image. The effect of stray light on cloud reconstruction was also explored by running the ART method with removing increasing portions of the circumsolar region. GHI and k errors were within 0.2% and 1% respectively when removing less than 30° around the sun.

Bibliography

[AJ96] Mark C. Allmen and W. Philip Kegelmeyer Jr. The computation of cloud-base height from paired whole-sky imaging cameras. *Journal of Atmospheric and Oceanic Technology*, 13(1):97–113, 1996.

[CLT13] MP Cadeddu, JC Liljegren, and DD Turner. The atmospheric radiation measurement (arm) program network of microwave radiometers: Instrumentation, data, and retrievals. *Atmospheric Measurement Techniques*, 6(9):2359, 2013.

[COAA08] A. Cazorla, FJ Olmo, and L. Alados-Arboledas. Development of a sky imager for cloud cover assessment. *JOSA A*, 25(1):29–39, 2008.

[COM$^+$05] Robert F. Cahalan, Lazaros Oreopoulos, Alexander Marshak, K. Franklin Evans, Anthony B. Davis, Robert Pincus, Ken H. Yetzer, Bernhard Mayer, Roger Davies, and Thomas P. Ackerman. The i3rc: Bringing together the most advanced radiative transfer tools for cloudy atmospheres. *Bulletin of the American Meteorological Society*, 86(9):1275–1293, 2005.

[CS08] Josep Calbo and Jeff Sabburg. Feature extraction from whole-sky ground-based images for cloud-type recognition. *Journal of Atmospheric and Oceanic Technology*, 25(1):3–14, 2008.

[CUL$^+$11] Chi Wai Chow, Bryan Urquhart, Matthew Lave, Anthony Dominguez, Jan Kleissl, Janet Shields, and Byron Washom. Intra-hour forecasting with a total sky imager at the uc san diego solar energy testbed. *Solar Energy*, 85(11):2881–2893, 2011.

[CWE97] Lin H. Chambers, Bruce A. Wielicki, and KF Evans. Accuracy of the independent pixel approximation for satellite estimates of oceanic boundary layer cloud optical depth. *Journal of Geophysical Research: Atmospheres*, 102(D2):1779–1794, 1997.

[Eva98] K. Franklin Evans. The spherical harmonics discrete ordinate method for three-dimensional atmospheric radiative transfer. *Journal of the Atmospheric Sciences*, 55(3):429–446, 1998.

[GBE$^+$12] Charlotte Gauchet, Philippe Blanc, Bella Espinar, Bruno Charbonnier, and Dominique Demengel. Surface solar irradiance estimation with low-cost fish-eye camera. In *Workshop on" Remote Sensing Measurements for Renewable Energy"*, 2012.

[GBH70] Richard Gordon, Robert Bender, and Gabor T. Herman. Algebraic reconstruction techniques (art) for three-dimensional electron microscopy and x-ray photography. *Journal of theoretical biology*, 29(3):471IN1477–476IN2481, 1970.

[GUC$^+$12] MS Ghonima, B. Urquhart, CW Chow, JE Shields, A. Cazorla, and J. Kleissl. A method for cloud detection and opacity classification based on ground based sky imagery. *Atmospheric Measurement Techniques*, 5(11):2881–2892, 2012.

[HEC$^+$07] Laura M. Hinkelman, K. Franklin Evans, Eugene E. Clothiaux, Thomas P. Ackerman, and Paul W. Stackhouse Jr. The effect of cumulus cloud field anisotropy on domain-averaged solar fluxes and atmospheric heating rates. *Journal of the Atmospheric Sciences*, 64(10):3499–3520, 2007.

[HES$^+$98a] Brent N. Holben, TF Eck, I. Slutsker, D. Tanre, JP Buis, A. Setzer, E. Vermote, JA Reagan, YJ Kaufman, and T. Nakajima. Aeroneta federated instrument network and data archive for aerosol characterization. *Remote Sensing of Environment*, 66(1):1–16, 1998.

[HES$^+$98b] Brent N. Holben, TF Eck, I. Slutsker, D. Tanre, JP Buis, A. Setzer, E. Vermote, JA Reagan, YJ Kaufman, and T. Nakajima. Aeroneta federated instrument network and data archive for aerosol characterization. *Remote Sensing of Environment*, 66(1):1–16, 1998.

[HHLL99] Annette Hammer, Detlev Heinemann, Elke Lorenz, and Bertram Lckehe. Short-term forecasting of solar radiation: a statistical approach using satellite data. *Solar Energy*, 67(1):139–150, 1999.

[HLW08] Dong Huang, Yangang Liu, and Warren Wiscombe. Determination of cloud liquid water distribution using 3d cloud tomography. *Journal of Geophysical Research: Atmospheres*, 113(D13), 2008.

[HM94] Lee Harrison and Joseph Michalsky. Objective algorithms for the retrieval of optical depths from ground-based measurements. *Applied Optics*, 33(22):5126–5132, 1994.

[HMS10] Anna Heinle, Andreas Macke, and Anand Srivastav. Automatic cloud classification of whole sky images. *Atmospheric Measurement Techniques*, 3(3):557–567, 2010.

[HTS^{+}01a] BN Holben, D. Tanre, A. Smirnov, TF Eck, I. Slutsker, N. Abuhassan, WW Newcomb, JS Schafer, B. Chatenet, and F. Lavenu. An emerging groundbased aerosol climatology: Aerosol optical depth from aeronet. *Journal of Geophysical Research: Atmospheres*, 106(D11):12067–12097, 2001.

[HTS^{+}01b] BN Holben, D. Tanre, A. Smirnov, TF Eck, I. Slutsker, N. Abuhassan, WW Newcomb, JS Schafer, B. Chatenet, and F. Lavenu. An emerging groundbased aerosol climatology: Aerosol optical depth from aeronet. *Journal of Geophysical Research: Atmospheres*, 106(D11):12067–12097, 2001.

[IP02] Pierre Ineichen and Richard Perez. A new airmass independent formulation for the linke turbidity coefficient. *Solar Energy*, 73(3):151–157, 2002.

[Jr94] WP Kegelmeyer Jr. *Extraction of cloud statistics from whole sky imaging cameras*, 1994.

[KLC05a] Evgueni Kassianov, Charles N. Long, and Jason Christy. Cloud-base-height estimation from paired ground-based hemispherical observations. *Journal of Applied Meteorology*, 44(8):1221–1233, 2005.

[KLC05b] Evgueni Kassianov, Charles N. Long, and Jason Christy. Cloud-base-height estimation from paired ground-based hemispherical observations. *Journal of Applied Meteorology*, 44(8):1221–1233, 2005.

[Kle13a] Jan Kleissl. *Solar energy forecasting and resource assessment*. Academic Press, 2013.

[Kle13b] Jan Kleissl. *Solar energy forecasting and resource assessment*. Academic Press, 2013.

[LHHB09] Elke Lorenz, Johannes Hurka, Detlev Heinemann, and Hans Georg Beyer. Irradiance forecasting for the power prediction of grid-connected photovoltaic systems. *IEEE Journal of selected topics in applied earth observations and remote sensing*, 2(1):2–10, 2009.

[Lil00] JAMES C. Liljegren. Automatic self-calibration of arm microwave radiometers. *Microwave Radiometry and Remote Sensing of the Earths Surface and Atmosphere*, pages 433–443, 2000.

[LSAD15] Aviad Levis, Yoav Y. Schechner, Amit Aides, and Anthony B. Davis. Airborne three-dimensional cloud tomography. In *Proceedings of the IEEE International Conference on Computer Vision*, pages 3379–3387, 2015.

[LSCP06] Charles N. Long, Jeff M. Sabburg, Josep Calb, and David Pags. Retrieving cloud characteristics from ground-based daytime color all-sky images. *Journal of Atmospheric and Oceanic Technology*, 23(5):633–652, 2006.

[MA04a] Roger Marchand and Thomas Ackerman. Evaluation of radiometric measurements from the nasa multiangle imaging spectroradiometer (misr): Twoand threedimensional radiative transfer modeling of an inhomogeneous stratocumulus cloud deck. *Journal of Geophysical Research: Atmospheres*, 109(D18), 2004.

[MA04b] Roger Marchand and Thomas Ackerman. Evaluation of radiometric measurements from the nasa multiangle imaging spectroradiometer (misr): Twoand threedimensional radiative transfer modeling of an inhomogeneous stratocumulus cloud deck. *Journal of Geophysical Research: Atmospheres*, 109(D18), 2004.

[MCBB11] M. Martnez-Chico, FJ Batlles, and JL Bosch. Cloud classification in a mediterranean location using radiation data and sky images. *Energy*, 36(7):4055–4062, 2011.

[MD05] Alexander Marshak and Anthony Davis. *3D radiative transfer in cloudy atmospheres*. Springer Science & Business Media, 2005.

[MDM03a] QL Min, M. Duan, and R. Marchand. Validation of surface retrieved cloud optical properties with in situ measurements at the atmospheric radiation measurement program (arm) south great plains site. *Journal of Geophysical Research: Atmospheres*, 108(D17), 2003.

[MDM03b] QL Min, M. Duan, and R. Marchand. Validation of surface retrieved cloud optical properties with in situ measurements at the atmospheric radiation measurement program (arm) south great plains site. *Journal of Geophysical Research: Atmospheres*, 108(D17), 2003.

[MH96a] Qilong Min and Lee C. Harrison. An adjoint formulation of the radiative transfer method. *Journal of Geophysical Research: Atmospheres*, 101(D1):1635–1640, 1996.

[MH96b] Qilong Min and Lee C. Harrison. Cloud properties derived from surface mfrsr measurements and comparison with goes results at the arm sgp site. *Geophysical Research Letters*, 23(13):1641–1644, 1996.

[MH16] Felipe A. Mejia and Laura M. Hinkelman. Coupling sky images with radiative transfer models: a new method to estimate cloud optical depth. *Atmospheric Measurement Techniques*, 9(8):4151, 2016.

[MHS89] K. McGuffe and A. Henderson-Sellers. Almost a century of imaging clouds over the whole-sky dome. *Bulletin of the American Meteorological Society*, 70(10):1243–1253, 1989.

[Miy64] Kenro Miyamoto. Fish eye lens. *JOSA*, 54(8):1060–1061, 1964.

[MK11] Patrick Mathiesen and Jan Kleissl. Evaluation of numerical weather prediction for intra-day solar forecasting in the continental united states. *Solar Energy*, 85(5):967–977, 2011.

[Mor06] VR Morris. *Microwave radiometer (MWR) handbook*, 2006.

[NK90] Teruyuki Nakajima and Michael D. King. Determination of the optical thickness and effective particle radius of clouds from reflected solar radiation measurements. part i: Theory. *Journal of the Atmospheric Sciences*, 47(15):1878–1893, 1990.

[NK14] Dung Andu Nguyen and Jan Kleissl. Stereographic methods for cloud base height determination using two sky imagers. *Solar Energy*, 107:495–509, 2014.

[NvWPC10] Sylvio Luiz Mantelli Neto, Aldo von Wangenheim, Enio Bueno Pereira, and Eros Comunello. The use of euclidean geometric distance on rgb color space for the classification of sky and cloud patterns. *Journal of Atmospheric and Oceanic Technology*, 27(9):1504–1517, 2010.

[OPW$^+$15] Daniel Oberlnder, Christoph Prahl, Stefan Wilbert, Sebastian Mller, Badrudin Stanicki, and Natalie Hanrieder. Cloud shadow maps from whole sky imagers and voxel carving. 2015.

[PE09] Robert Pincus and K. Franklin Evans. Computational cost and accuracy in calculating three-dimensional radiative transfer: Results for new implementations of monte carlo and shdom. *Journal of the Atmospheric Sciences*, 66(10):3131–3146, 2009.

[PML$^+$03] G. Pfister, RL McKenzie, JB Liley, A. Thomas, BW Forgan, and Charles N. Long. Cloud coverage based on all-sky imaging and its impact on surface solar irradiance. *Journal of Applied Meteorology*, 42(10):1421–1434, 2003.

[PYH$^+$15] Zhenzhou Peng, Dantong Yu, Dong Huang, John Heiser, Shinjae Yoo, and Paul Kalb. 3d cloud detection and tracking system for solar forecast using multiple sky imagers. *Solar Energy*, 118:496–519, 2015.

[RAC$^+$12] Roberto Romn, Manuel Antn, A. Cazorla, A. De Miguel, FJ Olmo, J. Bilbao, and Lucas Alados-Arboledas. Calibration of an all-sky camera for obtaining sky radiance at three wavelengths. *Atmospheric Measurement Techniques*, 5(8):2013, 2012.

[RHJ01] G. Roy, S. Hayman, and W. Julian. Sky analysis from ccd images: cloud cover. *Transactions of the Illuminating Engineering Society*, 33(4):211–221, 2001.

[SAK01] Malgorzata Szczodrak, Philip H. Austin, and PB Krummel. Variability of optical depth and effective radius in marine stratocumulus clouds. *Journal of the Atmospheric Sciences*, 58(19):2912–2926, 2001.

[SEPBA06] MP Souza-Echer, EB Pereira, LS Bins, and MAR Andrade. A simple method for the assessment of the cloud cover state in high-latitude regions by a ground-based digital camera. *Journal of Atmospheric and Oceanic Technology*, 23(3):437–447, 2006.

[SJK93] JE Shields, RW Johnson, and TL Koehler. Automated whole sky imaging systems for cloud field assessment. In *Fourth Symposium on Global Change Studies, American Meteorological Society*, pages 17–22, 1993.

[SPP78] Graeme L. Stephens, GW Paltridge, and CMR Platt. Radiation profiles in extended water clouds. iii: Observations. *Journal of the Atmospheric Sciences*, 35(11):2133–2141, 1978.

[SSF$^+$07a] G. Seiz, J. Shields, U. Feister, EP Baltsavias, and A. Gruen. Cloud mapping with groundbased photogrammetric cameras. *International Journal of Remote Sensing*, 28(9):2001–2032, 2007.

[SSF$^+$07b] G. Seiz, J. Shields, U. Feister, EP Baltsavias, and A. Gruen. Cloud mapping with groundbased photogrammetric cameras. *International Journal of Remote Sensing*, 28(9):2001–2032, 2007.

[Ste78] GL Stephens. Radiation profiles in extended water clouds. i: Theory. *Journal of the Atmospheric Sciences*, 35(11):2111–2122, 1978.

[TM04] Chaomei Lo Turner, David D. and Quilong Min. Cloud optical properties from the multi-filter shadowband radiometer (mfrsrcldod): An arm value-added product. 2004.

[V00] Tams Vrnai. Influence of three-dimensional radiative effects on the spatial distribution of shortwave cloud reflection. *Journal of the Atmospheric Sciences*, 57(2):216–229, 2000.

[YKN$^+$14a] Handa Yang, Ben Kurtz, Dung Nguyen, Bryan Urquhart, Chi Wai Chow, Mohamed Ghonima, and Jan Kleissl. Solar irradiance forecasting using a ground-based sky imager developed at uc san diego. *Solar Energy*, 103:502–524, 2014.

[YKN^{+}14b] Handa Yang, Ben Kurtz, Dung Nguyen, Bryan Urquhart, Chi Wai Chow, Mohamed Ghonima, and Jan Kleissl. Solar irradiance forecasting using a ground-based sky imager developed at uc san diego. *Solar Energy*, 103:502–524, 2014.

[YKN^{+}14c] Handa Yang, Ben Kurtz, Dung Nguyen, Bryan Urquhart, Chi Wai Chow, Mohamed Ghonima, and Jan Kleissl. Solar irradiance forecasting using a ground-based sky imager developed at uc san diego. *Solar Energy*, 103:502–524, 2014.